University of New Mexico
UNM Digital Repository

Mechanical Engineering ETDs | Engineering ETDs

Fall 11-15-2022

PARTICLE IMAGE VELOCIMETRY METHODOLOGY FOR CALCULATING THE ADVECTIVE LOSSES AT THE SOLAR TOWER FOR THE GEN 3 CONCENTRATED SOLAR POWER SYSTEM

Guillermo Anaya
University of New Mexico - Main Campus

Follow this and additional works at: https://digitalrepository.unm.edu/me_etds

 Part of the Mechanical Engineering Commons

Recommended Citation

Anaya, Guillermo. "PARTICLE IMAGE VELOCIMETRY METHODOLOGY FOR CALCULATING THE ADVECTIVE LOSSES AT THE SOLAR TOWER FOR THE GEN 3 CONCENTRATED SOLAR POWER SYSTEM." (2022).
https://digitalrepository.unm.edu/me_etds/220

This Thesis is brought to you for free and open access by the Engineering ETDs at UNM Digital Repository. It has been accepted for inclusion in Mechanical Engineering ETDs by an authorized administrator of UNM Digital Repository. For more information, please contact disc@unm.edu.

Guillermo Anaya

Candidate

Mechanical Engineering

Department

This dissertation is approved, and it is acceptable in quality and form for publication:

Approved by the Dissertation Committee:

Dr. Peter Vorobief , Chairperson

Dr. Gowtham Mohan

Dr. Clifford K. Ho

PARTICLE IMAGE VELOCIMETRY METHODOLOGY FOR CALCULATING THE ADVECTIVE LOSSES AT THE SOLAR TOWER FOR THE GEN 3 CONCENTRATED SOLAR POWER SYSTEM

by

GUILLERMO ANAYA

BACHELOR OF SCIENCE IN MECHANICAL ENGINEERING

UNIVERSITY OF NEW MEXICO, 2020

THESIS

Submitted in Partial Fulfillment of the
Requirements for the Degree of

Master of Science of Mechanical Engineering

The University of New Mexico

Albuquerque, New Mexico

December 2022

ACKNOWLEDGMENTS

I would like to acknowledge, Dr. Peter Vorobieff, my advisor and thesis chair, for all his support, patience, and advice throughout these years of research helping and supporting me achieve the milestones to be successful through my graduate studies.

I would also like to extend my gratitude to, Dr. Jesus Ortega, for all his support, advice, and guidance though this process and for providing me the opportunity to be part of his research from which this thesis has been made possible.

To Matthew Bauer and Andru Prescod from DOE for their management and support of this work, which was funded by DOE's Solar Energy Technologies Office (Award #33869). Sandia National Laboratories is a multimission laboratory managed and operated by National Technology and Engineering Solutions of Sandia, LLC., a wholly owned subsidiary of Honeywell International, Inc., for the U.S. Department of Energy's National Nuclear Security Administration under contract DE-NA0003525.

To the entire fluids laboratory team that welcomed me during my undergraduate studies and kept helping me through these times. I will forever be thankful to you folks.

Gratitude is extended to the Sandia National Laboratory, Concentrating Solar Technology Group for providing the used for the here presented research. To all the NSTTF technicians who collaborated and aid with the on-sun testing campaign.

To the ESS department for their support, to Elsa Castillo and Douglas Williams for their roll on connecting me with the CHRES program. To the CHRES program for the provided funding towards my studies. Thank you.

To my family, for all their support though all my academic career, for always motivating me to improve myself and to encouraging to pursue my dreams.

Lastly, thank you to my partner, Clarizza Morales, for always being there for me and for never letting me give up on my goals. For all the emotional support and advise that she has given me.

PARTICLE IMAGE VELOCIMETRY METHODOLOGY FOR CALCULATING THE ADVECTIVE LOSSES AT THE SOLAR TOWER FOR THE GEN 3 CONCENTRATED SOLAR POWER SYSTEM

by

Guillermo Anaya

B.S., Mechanical Engineering, University of New Mexico, 2020

M.S., Mechanical Engineering, University of New Mexico, 2022

ABSTRACT

The Falling Particle Receiver (FPR) built by Sandia National Laboratory (SNL) at the National Solar Thermal Testing Facilities (NSTTF) is one of the latest concentrated energy harvesting systems for Concentrated Solar Power (CSP). The FPR system at the NSTTF uses solid particles as both the heat transfer fluid and storage media. This FPR operates by having a gravity-driven particles curtain being irradiated through an open cavity by CSP, provided by a heliostat field. However, during operation plumes of particles being expelled out of the receiver cavity can be observed, resulting in heat losses as well as particle inventory losses. The work here presented describes the integration of Particle Image Velocimetry (PIV) techniques to sets of thermograms obtained from a high-speed IR camera for the development of a non-intrusive methodology aimed to estimate the advective losses of the mentioned FPR. To achieve this goal, both laboratory scale and field scale tests were conducted to validate the developed methodology.

Table of Contents

TABLE OF FIGURES

CHAPTER 1: INTRODUCTION

As the energy consumption demand keeps increasing around the world, more companies and entities are looking into the implementation of renewable energy systems as an alternative to fossil fuels to meet this ever-growing energy demand. Other factors to consider are the environmental impacts and the limited accessible supply of fossil fuels. In the other hand, renewable energy systems have the advantage of using replenishable/inexhaustible energy sources with an exceptionally low or, in some cases, inexistent impact to the environment. There exist multiple types of renewable energy systems, however, the one of interest for the here presented work is solar energy, one of the most abundant sources of renewable energy. Approximately 173,000 terawatts of solar energy strike the earth continuously. With that in mind, being able to capture just a small percentage of that energy would suffice to meet the world energy demand[1].

Multiple types of systems are being developed with the intention of taking advantage of such abundant resource; photovoltaic panels being the most popular one. Photovoltaic panels offer the convenience of transforming solar energy directly into electricity. However, most of the market available offer photovoltaic panels with an efficiency beginning at 6% to 20%. In photovoltaic panels most of solar energy is converted into waste heat, thus generating overheating problems that affect the efficiency of the system [2]. Another type of system used to take advantage of the energy provided by the sun are solar collectors that transform solar radiance into thermal energy. Some of these systems allow for thermal energy collection at temperatures above 600℃, which allows for higher operational efficiencies. An example of these systems are the central receivers for Concentrated Solar Power (CSP) [3]–[5].

Figure 1: Heliostat field and central solar tower at Sandia's NSTTF with soldid particle reciever mounted on top of the tower.

The interest in the field of CSP has been in the rise in the last few decades as it is used on different types of receivers, like those using falling solid particles [6]. An example of this system can be found at the Sandia National Laboratories (SNL) National Solar Thermal Testing Facility (NSTTF) shown in Figure 1, where they built a falling particle receiver (FPR). This falling particle receiver forms part of the CSP Gen3 program issued by the Department of Energy (DoE) and designed by SNL. It offers a favorable path to operating temperatures up to and above 700℃, with heat fluxes greater than 1 MW/m^2 by implementing the use of synthetic Silica-based bauxite particles of sub-millimeter size as heat transport and storage media. Additionally, the heat stored in these particles can be later used as input transferring heat into a supercritical carbon dioxide (s-CO2) Brayton power cycle, capable of yielding a thermal-to-electric conversion efficiency equal or greater than 50% [3]–[5], [7], [8]. Also the use of inert particles as the heat transport (HTF) fluid offers significant advantages over more conventional HTFs, such as molten nitrate salts, expanding the ranges of operating temperatures from subzero to > 1000℃ compared to about 200℃ to 600℃ for nitrate molten salt, along with cost, low corrosion effects, and no need to high level air-tight seals [9], [10].

The falling particle receiver at Sandia faces one of its greatest challenges during operation. Due to multiple factors and weather conditions, plumes of particles are being expelled out of the receiver aperture during on-sun and off-sun operation which can lead to significant material and heat losses for the system (Fig. 2).

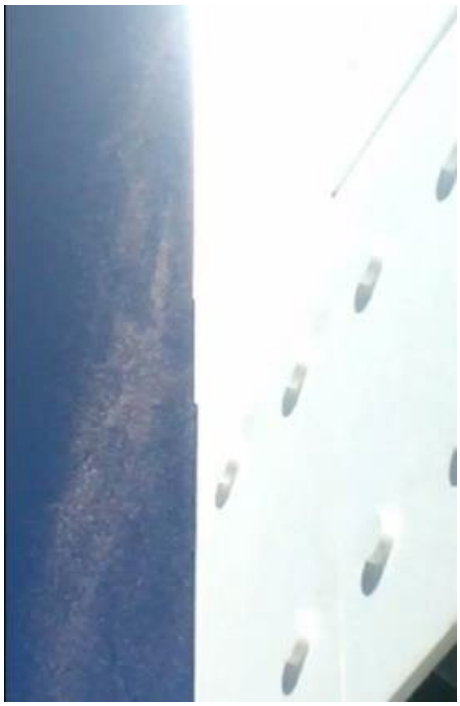

Figure 2:Particle egress captured from the falling particle receiver aperture during on-sun testing. [[7], [11]–[16]]

The main purpose of the work conducted and here presented is to establish a methodology to calculate the egress flow rate of particles being expelled out of the FPR cavity. With this methodology, the goal is to also present its aid in the calculation of the advective losses of the system through the uses of Particle Image Velocimetry (PIV) techniques and tools.

CHAPTER 2: PIV STUDIES

2.1 PIV Overview

Particle Image Velocimetry is a technique used to extract velocity vector fields in one or two dimensions from a flow using time-resolved sequences of images. For most cases, in order to implement PIV tools, it is required to either seed the flow of interest or to use a laser bed. This is needed in order to identify the particles of interest and enable the PIV packages to track the particles and produce the velocity vectors [17], [18].

Velocity vector fields are obtained by analyzing a region of interest (ROI), which can be set by the user to focus the analysis on a particular zone present in the field of view captured by the used cameras. This method is often implemented to reduce the computational time and/or to reduce the presence of non-useful velocity vector field form outside the area of interest (Setting the ROI varies depending on the PIV package being use for the analysis). Focusing on the ROI, the sets of consecutive images are analyzed to detect the motion in clusters of pixels (Figure 3). Depending on the PIV package used, the PIV software might identify the clusters of moving pixels by using signal filtration through either Direct Fourier Transform (DTF) or a series of algorithms denominated as Fast Fourier Transform (FFT) methodology. Implementing the discrete form of a Fourier transform (i.e. DTF or FFT) for the image processing leads to new images where only the frequencies for the particles of interest remain in the image, while the rest is filtered out [19], [20].

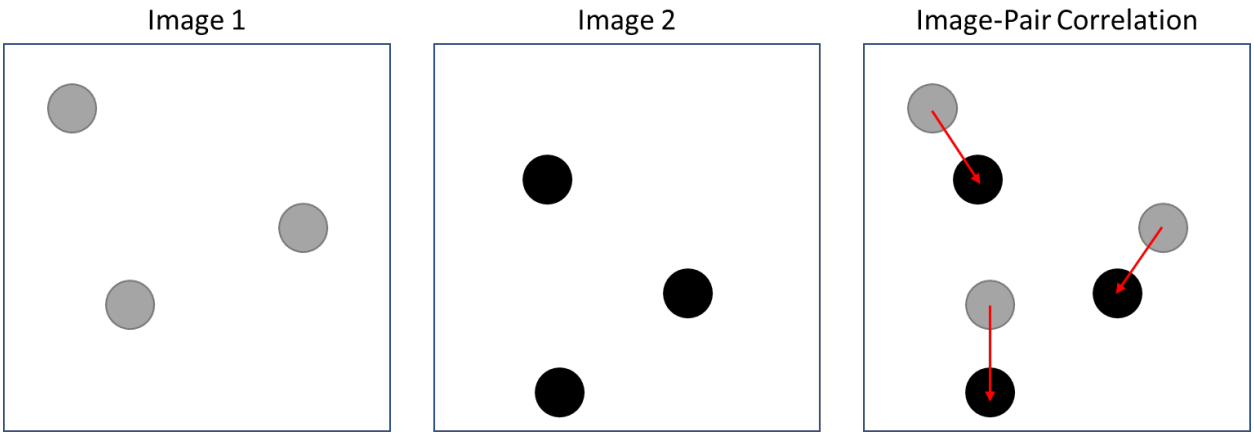

Figure 3: Correlation of particles within the ROI to establish velocity vectors due to the displacement of pixel clusters [13].

Then, to obtain the respective velocity vectors the sets of images are subjected to a cross-correlation process. It should be noted that some PIV software might skip over the filtering of the images and apply a Direct Cross-Correlation. For two discretely sampled images the cross-correlation function is defined as follows:

$$\Phi_{fg}(m,n) = \sum_{i}\sum_{j} f(i,j) \times g(i+m, j+n) \tag{1}$$

Here $\Phi_{fg}(m,n)$ is the cross-correlation function, $f(i,j)$ and $g(i,j)$ represent the image intensity distribution of the first and second image correspondently, and m and n represent the pixel offset between the two images [21]. Once the pixels offset is obtained, the velocity vectors can be calculated by using calibration factors. These factors include pixel-to-distances and time-resolution between images, as well as other user pre-specified conditions for the analysis. Using this information, the PIV software performs a reinterpretation of the velocity vectors to provide a more useful representation of the velocities on the desired units of measurement [22].

2.2 PIV Applications

Particle Image Velocimetry techniques have a broad range of applications ranging from applications on the micro-scale [23] to solid particle flow characterization [7], [16], [17]. The following are brief descriptions of how the PIV techniques have been used for different applications and studies.

In 2007 a study conducted at the University of Cambridge used PIV to study the motion of a single bubble as it approached and then broke through the top surface of a two-dimensional gas-fluidized bed. The goal was to obtain a complete set of velocity vectors around the bubble as it broke through the surface. The study revealed that the vorticity around the bubble is close to zero (except for the region at the bottom of the bubble) justifying the use of potential flow theory to predict the bubble motion around the bubble. The use of PIV also helped to reveal that even after eruption, the potential flow theory provided an adequate prediction of the velocities of particles from the ruptured roof of the bubble [24].

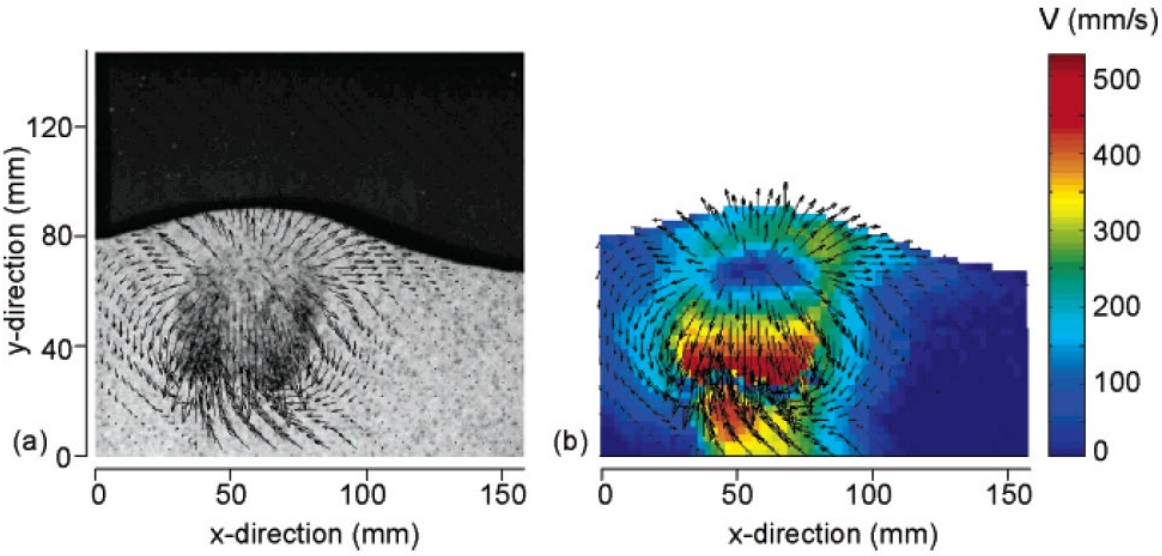

Figure 4: Bubble approaching the top of a 2D fluidized bed. (a) Bubble and particulate phase as seen by the camera, with arrows indicating the velocity. (b) Same as (a) with colors added to indicated velocity magnitudes [24].

Other examples with different applications of PIV include the study conducted by the Department of Aerospace Engineering at the Delft University of technology. Here they reviewed an approach for extracting pressure fields from a flow velocity field data obtained using PIV techniques by combining the experimental data with governing equations. This study lead to a diagnostic methodology for determining the instantaneous flow field pressure in a non-intrusive way[25]. PIV has also been used on studies on the micro-scale, like the study conducted at Technische Universität t Braunschweig, in Germany [26], and the study from the Department of Electrical and Computer Engineering from the Beckman Institute for Advanced Science and Technology [23]. In both studies, the PIV techniques were implemented to develop micro-resolution PIV systems. The first mentioned, used these techniques with the intention to measure wall-shear-stress and the near-wall flow properties, and the latter to measure velocities in a Hele-Shaw flow around a 30 μm elliptical cylinder [23], [26].

Particle Image Velocimetry has also been used to analyze the mixing of a two-phase flow. The University of Karlsruhe conducted an experiment where they looked at the interaction between spray droplets from an injector and the ambient air by means of a two-phase PIV analysis [18]. Along with studies focused on the characterization of solid particle flows, including dynamic analysis of granite rock burst [27] and characterization of gravity driven solid particle flows [7].

CHAPTER 3: METHODOLOGY

3.1 PIV Software Used

As previously mentioned in chapter two, Particle Image Velocimetry is an imaging technique used to extract complete velocity vector field in one- or two-dimensions using time-resolved image sequences. The goal here is to use PIV and apply it thermogram sequences to determine a correlation between the thermograms to extract the bulk velocity from a curtain of Silica-based bauxite falling particles, which was heated at different temperatures. The reason for extracting particles bulk velocities instead of velocities of single particles originates from the resolution capabilities of the equipment used and the size of the particles of interest.

There exist multiple different PIV pages like OpenPIV, PIVview, DaVis, PIVlab, JPIV, DigiFlow, and many other available either through opensource coding or by buying a license to obtain a commercial software. Most of them follow a similar process as the one described in section 2.1 to extract the velocity vector fields.

To assure we would obtain reliable PIV data, two different PIV packages were implemented. The first image used was DaVis, a commercially available and trusted PIV software. The second one was a MATLAB toolbox known as PIVlab, which has been used on different studies in the past [28]. PIVlab will be the primary analysis tool for extracting velocity vector fields through PIV, the DaVis software, which have been validated for a wide range of applications. PIV and PTV will be used to validate the reliability of PIVlab for the experiments conducted at the University of New Mexico (experiments presented on section 4.1). PIVlab toolbox along with DaVis software were used to extract falling solid particles bulk velocity without using laser beds nor seeding the flow. The resulting vector fields will be compared to the expected results based on study characterization of gravity driven particle flow done at the Sandia National Laboratories [8]. This experiment

showed that for a curtain of small falling particles, the particle's velocities follow the behavior of spherical particles in free-fall without experiencing drag.

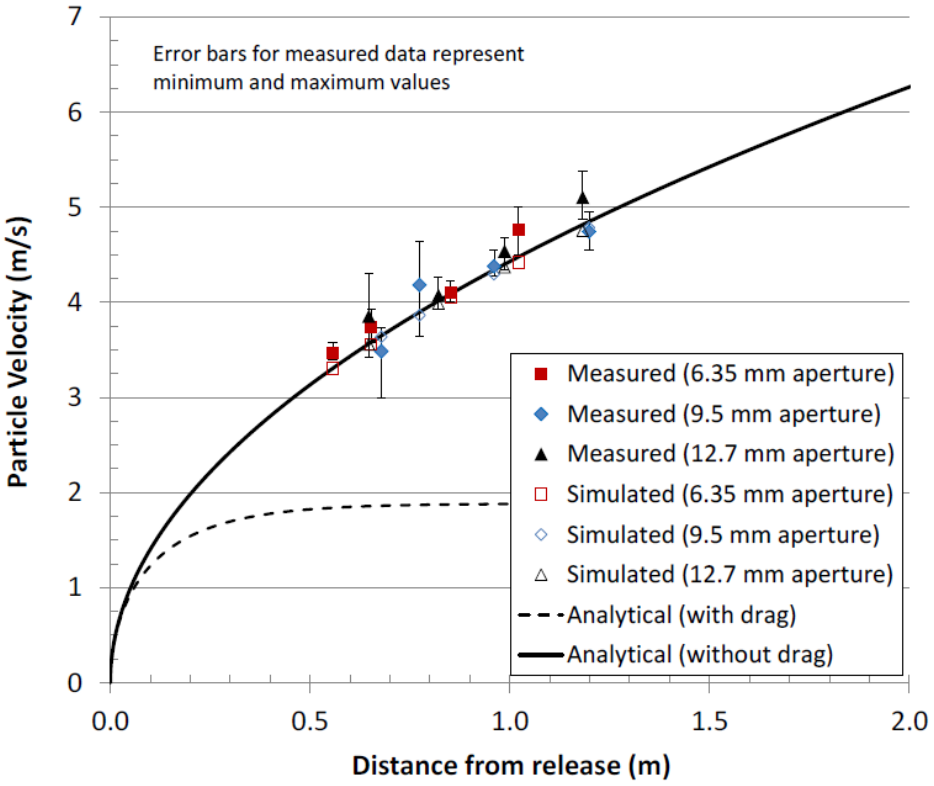

Figure 5: Measured, simulated (Ansys Fluent), and analytically modelled particle velocities [8].

3.2 PIVlab

PIVlab can be run using either the Graphic User Interface (GUI) or by directly running its respective MATLAB script (note: PIVlab requires the MATLAB image processing toolbox to run). Using the PIVlab GUI makes running this type of analysis easily accessible to everyone since most of the functions related to PIV can be accessed through it. To perform the analysis only three major steps are needed(image pre-processing, image evaluation, and post processing) [22]. However, the PIVlab GUI was only used for the processing of the experiments conducted at the

UNM facilities, while for the processing of the experiments conducted at the NSTTF PIVlab was ran directly from the MATLAB script to optimize processing time.

The PIVlab analysis for the experiments carried at the UNM solar simulator facilities was conducted as follows. First, a region of interest was established containing the curtain of falling particles. This was done to limit the processing to the desired ROI and avoid any unnecessary extra processing. Figure 6 shows the established ROI. Moving on, the second step was image pre-processing (which is one of the three major steps for the analysis). Here the settings were left as the default setting for PIVlab, meaning that a Constant-Limited Adaptive Histogram Equalization (CLAHE) was the used technique for pre-processing of the images (or thermograms).

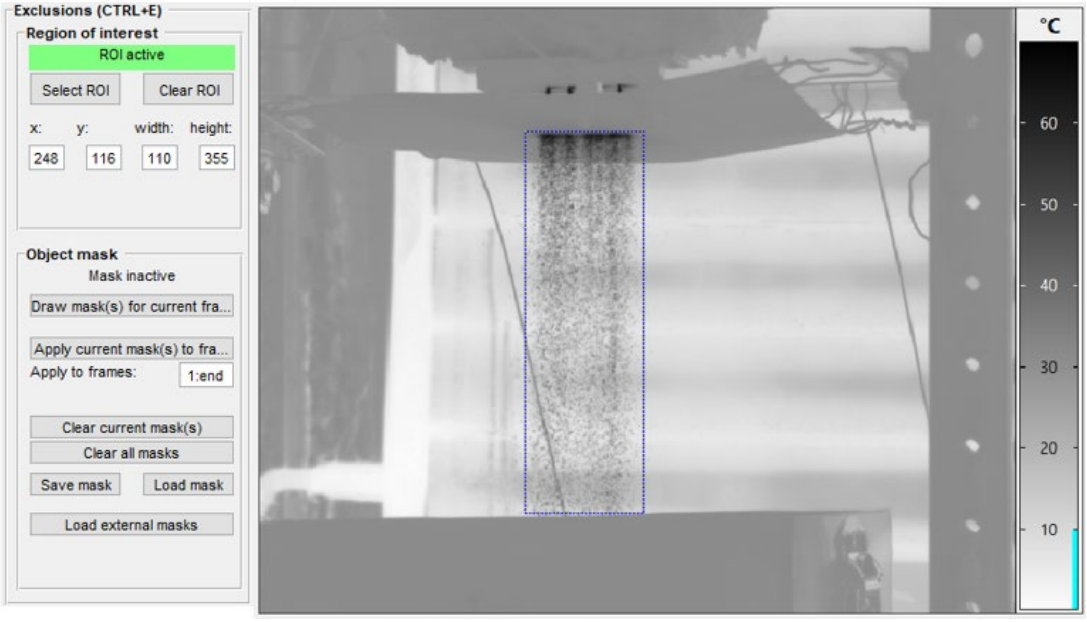

Figure 6: Establishing region of interest for the PIV analysis. [13]

Following the pre-processing setup, the calibration factors were provided to generate the conversion factors from pixel distance to physical distance, as well as the time steps between each image. To obtain the pixel distance to physical distance two known reference points were used. In

this case, the perforations on the structure shown to the right were used since it was known that each perforation is two inches (2”) apart from each other (Figure 7). For the time step calibration, the shooting frequency of the camera used was 300 Hz ≈ 3.333 milliseconds.

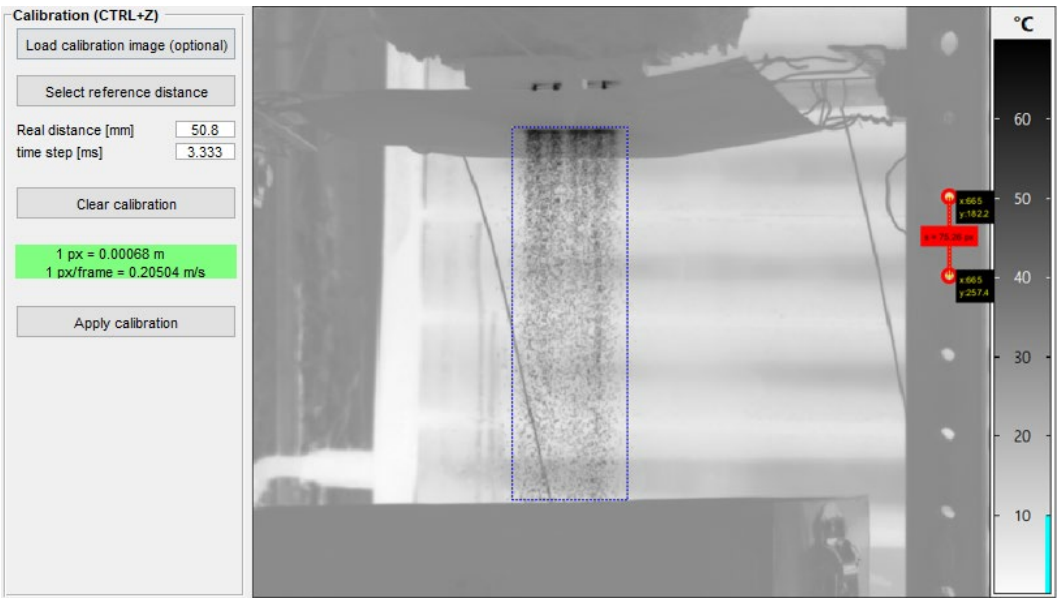

Figure 7: PIVlab Calibration process used to establish the physical conversion parameters. Red line shows the perforations on the structure used for the calibration. [13]

The next step to follow was image evaluation. For PIVlab this step can be accessed on the PIV settings under the analysis tab. Here it is possible to select between three types of PIV algorithm, as well as how many passes will be performed during the PIV analysis. During this step, the FFT window deformation PIV algorithm was selected along with multiple passes and interrogation areas with 50% steps. The interrogation areas used were square areas with side length of 32, 16, and 8 for pass 1, pass 2, and pass 3 respectively and the rest of the available settings were left as default for PIVlab (Figure 8).

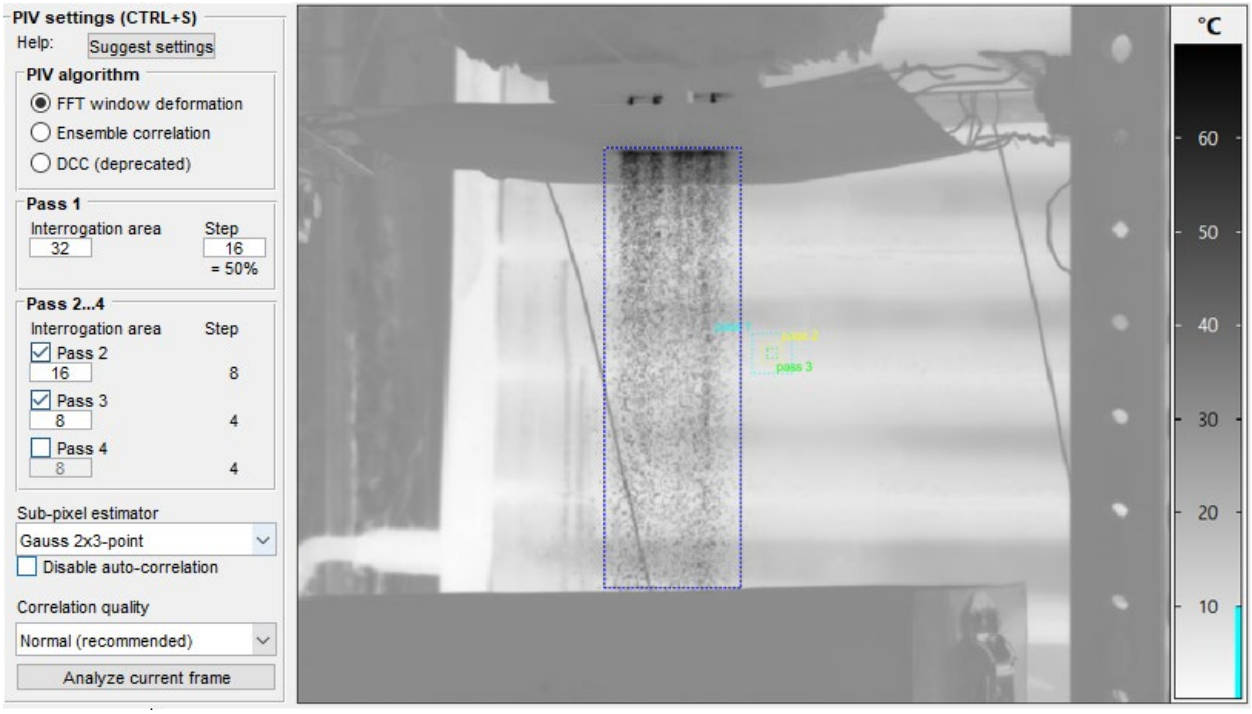

Figure 8: PIVlab Image evaluation settings used. [13]

Lastly, PIV post-processing settings were kept as the default settings provided by PIVlab with a standard deviation threshold of seven. Once all the settings were introduced into PIVlab on the corresponding location, the full analysis was performed yielding the velocity vector for the bulks of falling particles.

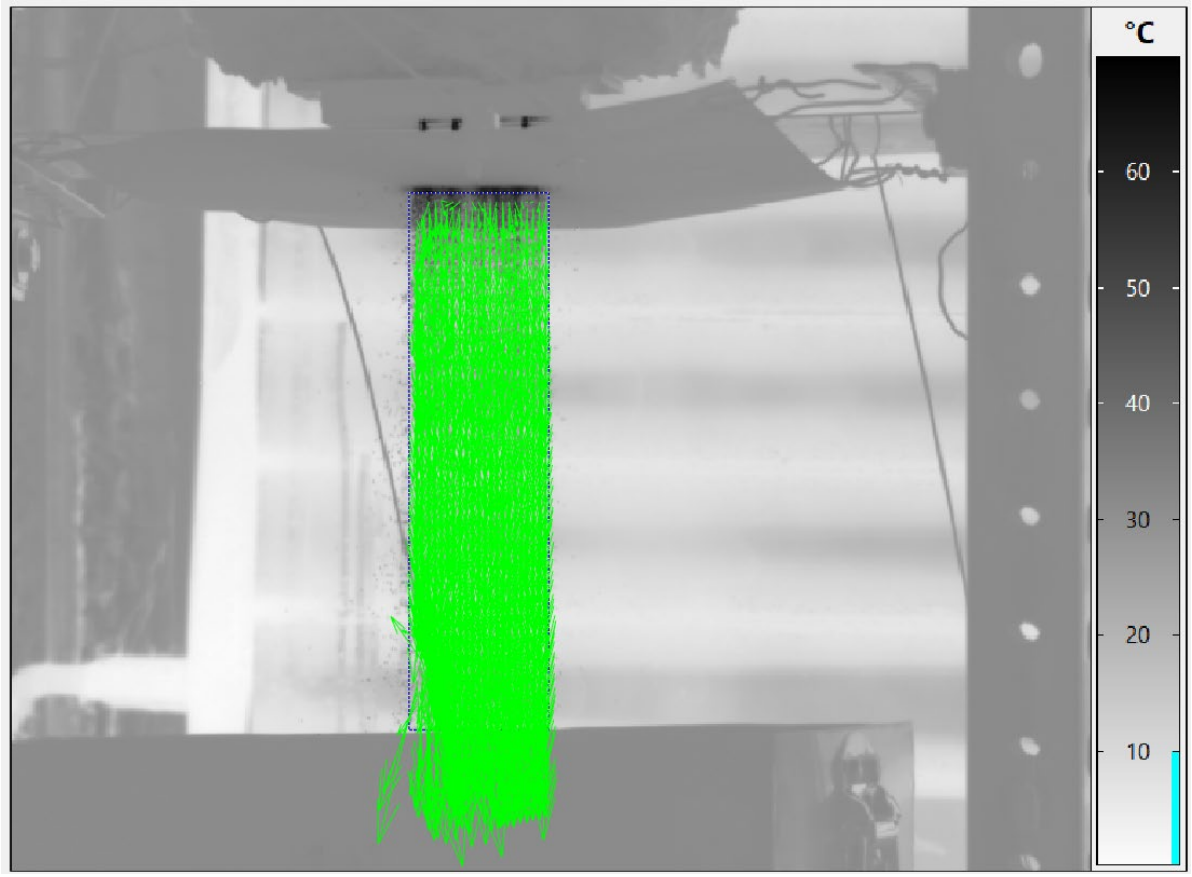

Figure 9: Velocity vectors field optioned from the PIVlab analysis. [13]

Thanks to its user-friendly interface and accessibility, PIVlab is rising in popularity as a PIV tool and has been used on multiple studies like “gas migration regimes and outgassing in particle-rich suspensions”[29], “transition from turbulent to coherent flows in confined 3D active fluids” [28], and “particle velocimetry analysis of immiscible two-phase flow in micromodels” [30], among others.

Due to the nature of the overall post-processing steps and the compatibility of PIVlab with the main processing code written on MATLAB, PIVlab was chosen to be the most efficient and convenient PIV technique. Using PIVlab allowed for an overall integration for calculating the advective losses of the system.

CHAPTER 4: THEORY AND EXPERIMENTATION

4.1 Theory

The overall goal for the project is to develop a methodology to calculate the egress mass flow rate of particles form the falling particles receiver and thus calculate the advective losses of the system. Mass flow rate can be calculated as shown on Eq. 2. The methodology here presented will be focusing on obtaining the velocity component for the calculation of the egressing mass flowrate using PIV techniques

$$\dot{m} = \rho_b A_c V_b \tag{3}$$

Where ρ_b is the bulk density of the plume, A_c is the cross-sectional area of the flow, and V_b is the bulk velocity of the flow. For obtaining the bulk velocity it has be proven that it can be measured from the use of sets of high speed thermograms using PIV techniques, as shown by Dr. Ortega et al [13], [15], [16]. In a similar manner, the cross-sectional area of the plume can be estimated by using images from which the width, w_c, and thickness, t_c, of the plume can be computed [13], [16]. Implementing this into Eq. 3 yield to Eq. 4 for calculating the mass flow rate.

$$\dot{m} = \rho_b w_c t_c V_b \tag{4}$$

As there is not direct nor indirect method to calculate the bulk density, one can then use the method developed by Ortega et al [7], [13], [14], [31], [32] where the density of the plume can be calculated by implementing a series of opacity based calculations utilizing a modified version of the Beer's law presented by Kim et al describing a correlation between opacity, ω, volume fraction of the plume, ϕ_p, shown on Eq. 5, and curtain thickness, τ, shown in Eq. 6 [13], [17].

$$\phi_p = \frac{\rho_b}{\rho_p} \tag{5}$$

$$\omega = 1 - e^{-\frac{3\phi_p \tau}{2D_p}} \tag{6}$$

Combining Eq. 5 and Eq. 6 leads to one single equation to determine the bulk density of the plume as a function of opacity shown in Eq. 7 [12], [17].

$$\rho_b = -\frac{2D_p \rho_p}{3\tau} \ln(1-\omega) \tag{7}$$

For further simplification one can combine Eq. 5 and 7 to obtain a final equation for calculating the mass flow rate as a function of only two unknown variables: opacity and bulk velocity of the plume.

$$\dot{m}_p = \left(-\frac{2D_p \rho_p}{3\tau} \ln(1-\omega)\right) w_c t_c V_b \tag{8}$$

Considering that

$$t_c = \tau \tag{9}$$

Equation 8 can be further simplified to eliminate the need for calculating the thickness of the plume, Eq. 10 [12], [13], [16].

$$\dot{m}_p = -\frac{2}{3} D_p \rho_p \ln(1-\omega)\, w_c V_b \tag{10}$$

Thus, as demonstrated by Dr. Ortega et al ([12], [13], [16]) it is possible to obtain the bulk velocity of a the particle plume/curtain by using high speed IR camera and implementing PIV imaging techniques. Meanwhile the opacity can be determined from the images obtained using the visual light camera, and the rest of the parameters needed to determine the mass flow rate are known properties values of the particles conforming the plume. Then, the calculated mass flow

rate can be used to determine the heat losses of the system, Eq. 11, if the particle heat capacity is known, and the particles temperature can be measured.

$$\dot{\mathrm{Q}}_p = \dot{m}_p \int_{T_{amb}}^{T_p} Cp_p(T)dT \tag{11}$$

Moreover, another aspect of interest for calculating the advective losses of the falling particle receiver system is the heat loss component carried by the air egressing from the cavity along with the plume of particles. In an equivalent manner to that of the particles plume, the heat component being carried out by the air can be estimated using Eq. 13. In the equation, the particles can be used as tracers to determine the velocity of the air, Eq. 12, and the temperature of the air can be assumed to be that of the plume. [11], [12]

$$\dot{m}_a = \rho_a T_p A_c V_b \tag{12}$$

$$\dot{\mathrm{Q}}_a = \dot{m}_a \int_{T_{amb}}^{T_a} Cp_a(T)dT \tag{13}$$

Hence, the overall advective losses of the FPR can be expressed as the sum of the heat losses being carried out by the particles and the air egressing from the cavity. Eq. 13 [11].

$$\dot{Q}_A = \dot{Q}_a + \dot{Q}_p \tag{14}$$

Where $\dot{Q}_A$ represents the total advective of the FPR.

4.2 Hot Flow Experiments at The University of New Mexico Facilities

For this project multiple set of experiments were conducted at the University of New Mexico Solar simulation facilities. The objective of the experiments conducted here was to

evaluate the developed methodology, and to calibrate processing code to build confidence on its capabilities to determine the mass flow rate using only imaging techniques.

4.2.1 Experimental Set Up

The experimental set-up used at the University of New Mexico Solar Simulator consisted of the following components. An actuated furnace used to heat up the particles to the desired temperature for the experiment. A top hopper with an exchangeable bottom perforated plate for particles flow control and equipped with thermocouples to measure the temperature of the particles exiting the furnace. A sling gate intended to start and stop particles flow. An interchangeable metallic mesh used to moderate the flow and provide a semi-uniform plume of falling particles. A bottom hopper to collect falling particles equipped with thermocouples to measure the final temperature of the particles after falling. Lastly, the high-speed IR camera used is an ImageIR® 8300 hp with a 100mm lens at a resolution of 640X512 pixels situated five meters from the particles curtain, as it would be the distance at which it will be located when testing at the NSTTF on SNL. It should be noted that at this distance the pixel size is estimated to be 750 μm [32].

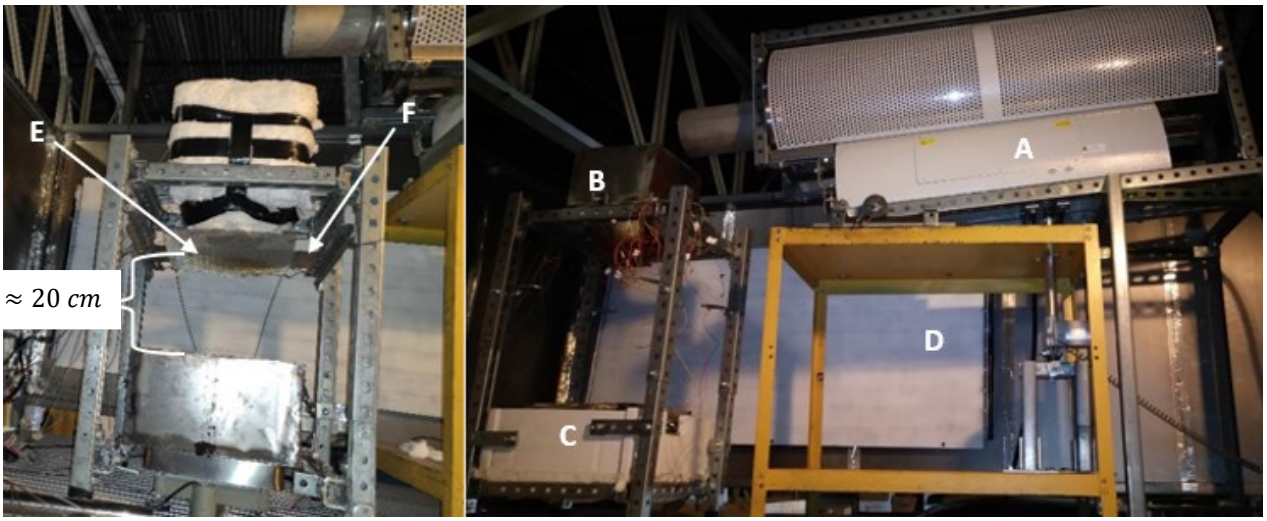

Figure 10: Experimental set up used at UNM Solar simulator facilities. The components are the following: A) Furnace. B) Top hopper. C) Bottom hopper. D) Cooled panel. E) Metallic mesh. F) Sliding gate. [12], [13]

Figure 11: The ImageIR® 8300 hp, using a 100mm lens at a resolution of 640X512 pixel was used to obtain the sets of thermograms.

The main reason for using this high-speed IR camera was to extract the plum's temperature as a function of time; however, if the temporal resolution is sufficient, it can also be used to estimate the bulk particle motion from the obtained sequences of thermograms using PIV. Thus, the IR camera will serve two purposes, 1) to measure the particle temperatures and 2) to measure the bulk particles velocity as a function of position for the calculation of the mass flowrate. The

ImageIR® 8300 hp is capable of shooting at a 300 Hz allowing for 300 thermograms per second. Taking advantage of this, during each test we were able to obtain multiple sets of thermograms to later analyze and extract the desired information, particle temperature and velocity. Each set consisted of 300 thermograms taken with a time difference of 3.333 milliseconds.

4.2.2 Experimental Tests and Results

A set of tests were performed where about 5 Kg of particles were pre-heated to 6 different temperatures (i.e., 100°C, 200°C, 300°C, 450°C, 600°C, and 750°C) in the actuated furnace, to then be poured into the top hoper, where the heated particles were held until all the equipment and members of the team were ready to proceed with the testing. Once all the Data Acquisition systems were ready, the sliding gate was opened allowing for the particles to go through the restraining flow metallic mesh producing the curtain of falling particles. Once the curtain was formed, multiple sets of recording were captured using the IR camera and a visual camera to later be analyzed.

Performing the experiments had two main objectives. The first objective was to evaluate the fishability of using the high-speed IR thermograms to extract the bulk temperature of the falling particles. The second goal was to apply PIV to these thermogram sequences to obtain the bulk velocity of the particles in the plume. After each experiment was recorded with the high-speed IR camera, the sets of 300 thermograms were extracted from the software used to control the IR camera as .ASCII files in grey scales, and later transformed into .tiff images for compatibility with the PIV packages.

The acquired thermograms were subjected to a PIV analysis through both, PIVlab and DaVis. The method described in section 3.2 was used for the PIVlab analysis. The DaVis software

analysis was conducted in an equivalent manner. A ROI containing the curtain of falling particles was established. The pre-processing of the images was kept as the default settings provided by the software. The same point of reference and time steps were provided for the calibration of the system. A similar FFT algorithm with multi-pass evaluation of the images was set, like the one for the PIVlab analysis. Lastly, the post-processing setting were kept as the default setting provided by the DaVis software.

Once both PIV analyses were conducted, the next step was to compare them. First, they were compared to the expected results based on previous studies conducted on curtains of falling particles [8]. Secondly, they were compared to the PIVlab and DaVis results to evaluate the fidelity of the PIVlab.

Based on the results obtained on the study of "Characterization of particle flow in free-falling solar particle receiver" [8] the particles should present free-fall like behavior governed by the following equation:

$$V_p = \sqrt{2 * g * \Delta y} \tag{15}$$

Where V_p is the particle velocity, Δy is the displacement of the particle from the discharging point, and g represents the gravitational acceleration ($9.81 m/s^2$). Thus, the velocity region for the experiment is expected to have maximum velocities around $2.1\ ^{m}/_{s}$ due to the fall distance of 0.25 meters.

To accomplish the comparison between the expected velocities and those obtained from the PIV analyses, the following was done. Polylines of data from the discharging pint to the bottom of the particle curtain were extracted from the resulting vector fields to compare them the expected behavior governed by equation 2. It is noted to mention that only the vertical component of the

velocities was extracted for this analysis as it is the only component of interest for the comparison with expected velocity values. A small comparison was performed using PIVlab to determine if the location of the polyline on the curtain signified any significant variance on the vertical velocity across the width of the curtain. To execute this analysis three vertical lines at various locations were chosen to be compared on the mean velocity field of a set (450 °C, 3-5 g/s, single curtain).

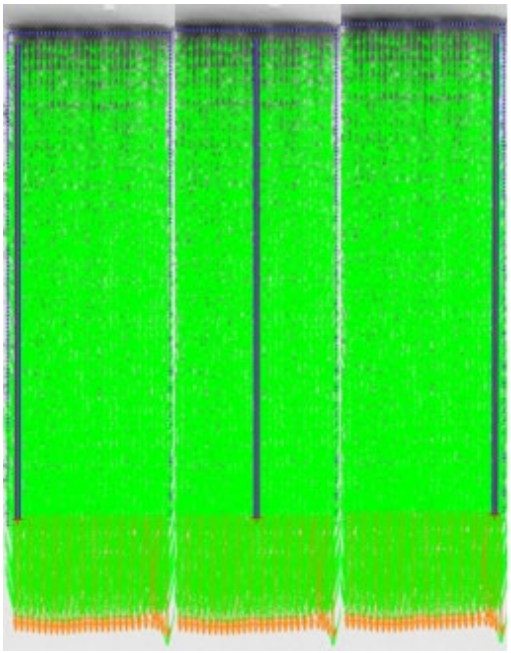

Figure 12: Velocity as a function of discharge position can be extracted from the vector field using pre-specified linear paths. Here the three postions used to extract the velocity profiles across the curtain thicknes.[15]

As shown in Figure 13, the comparison of the different velocity profiles across the curtain of falling particles led to the conclusion that there are no considerable discrepancies between the velocity profiles within the curtain. Thus, it is safe to assume that a horizontal variation on location for the extracting polyline has negligible effects on for the variation of the vertical velocities on the curtain. Moreover, this allows us to determine that the velocities extracted from the center line

are representative values of the horizontal average velocity of the curtain at any given point along the y-axis.

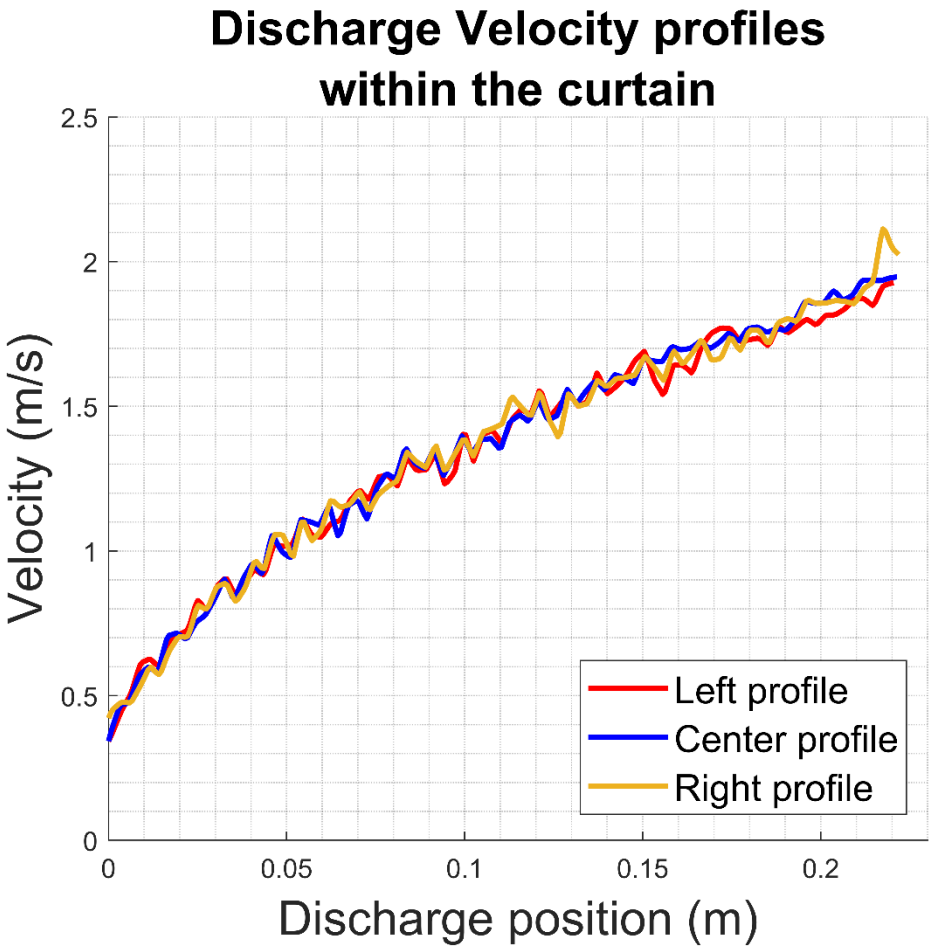

Figure 13: Comparison of the three velocity profiles along the curtain thickness.

Since the variance of velocity across the curtain is negligible, as previously mentioned, only the velocities from the center line were extracted moving forward as they can be assumed to represent the average velocity at the given falling position on the curtain. Next, the effects of the temperature were analyzed and compared at different mass flow rates and curtain shapes using both PIVlab and DaVis.

Now, to compare the velocity profile from the center line with the expected velocities as a function of position three representative experiments were selected. The selected cases were conducted at 100℃, 450℃, and 750℃ with a measured mass flowrate of about 5 g/s. Thanks to the compatibility and ease of use, the PIVlab data was easy to extract and analyze. PIVlab offers the option of extraction just the velocities corresponding to the pre-stablished polyline into text file than can be later read by MATLAB and use for the analysis. The comparison of the center line polyline with the expected velocities yields the following graphs (Figures 14-16).

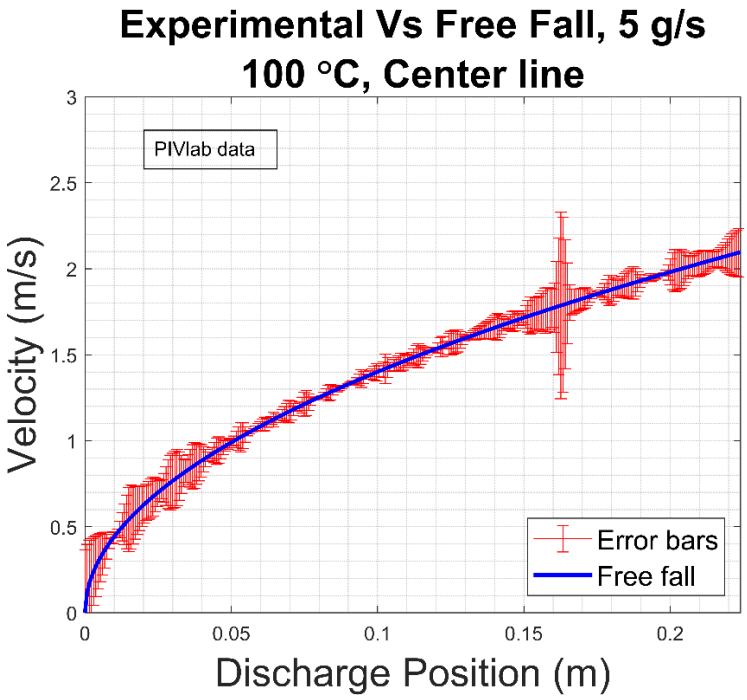

Figure 14: Discrepancies between the velocity profile from the center of the particle curtain and the expected free fall behavior at 100℃. PIVlab analysis data.

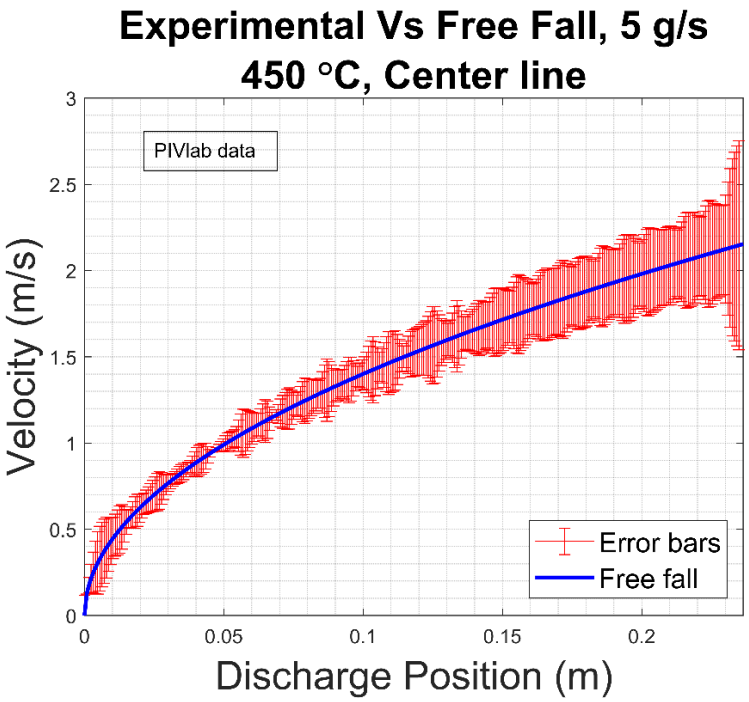

Figure 15: Discrepancies between the velocity profile from the center of the particle curtain and the expected free fall behavior at 450°C. PIVlab analysis data.

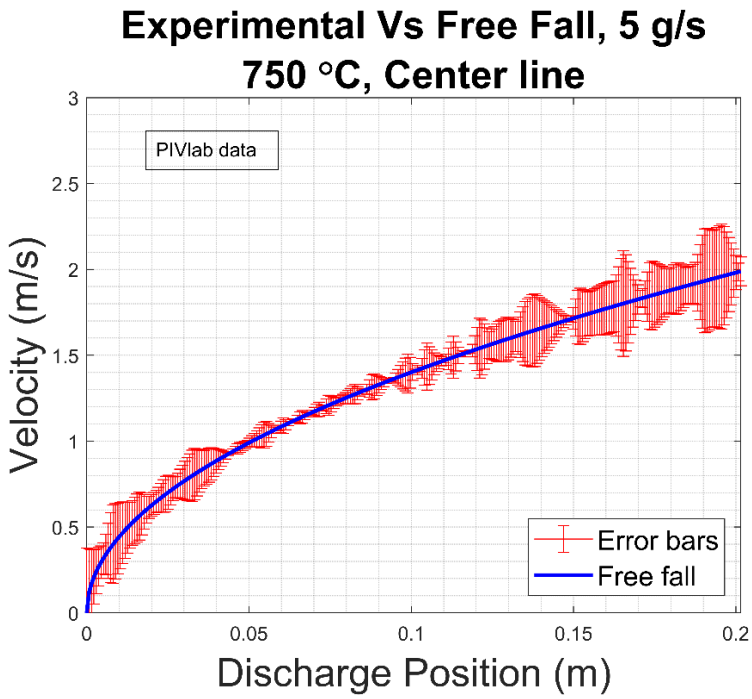

Figure 16: Discrepancies between the velocity profile from the center of the particle curtain and the expected free fall behavior at 750°C. PIVlab analysis data.

As a verification method, a similar procedure was followed to conduct a similar comparison with the data obtained from performing the PIV analysis through the DaVis software. Unlike PIVlab, DaVis software did not allowed for the direct extraction of just the desired data from a pre-set polyline. Thus, the PIV analysis date was extracted as a .DAT file containing the velocity information for the entire analyzed image instead of just the vector field from the ROI. To extract the velocity data corresponding to the center line of the curtain a "cleaning" MATLAB script was developed (Appendix A), resulting on the following graphs (Figure 17-19) for similar comparison as that conducted for the PIVlab cases.

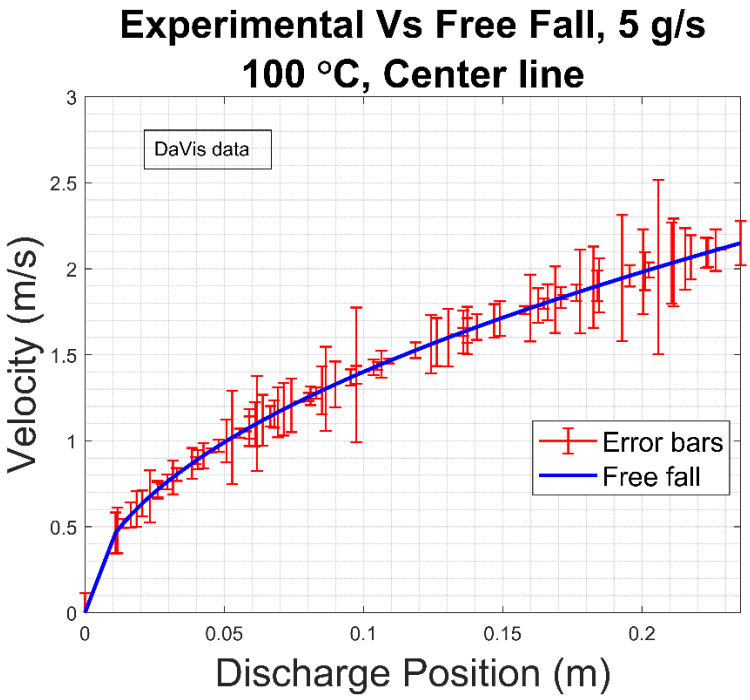

Figure 17: Discrepancies between the velocity profile from the center of the particle curtain and the expected free fall behavior at 100°C. DaVis analysis data.

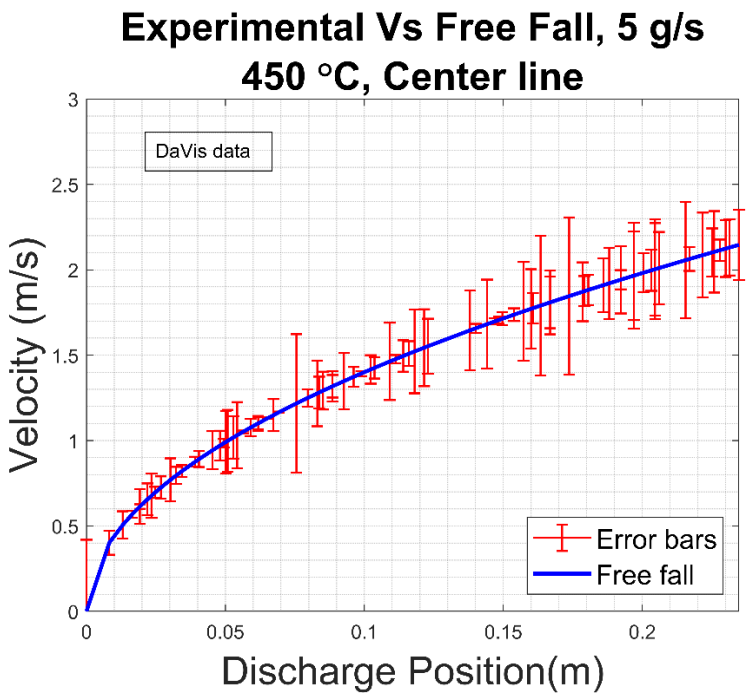

Figure 18: Discrepancies between the velocity profile from the center of the particle curtain and the expected free fall behavior at 450°C. DaVis analysis data.

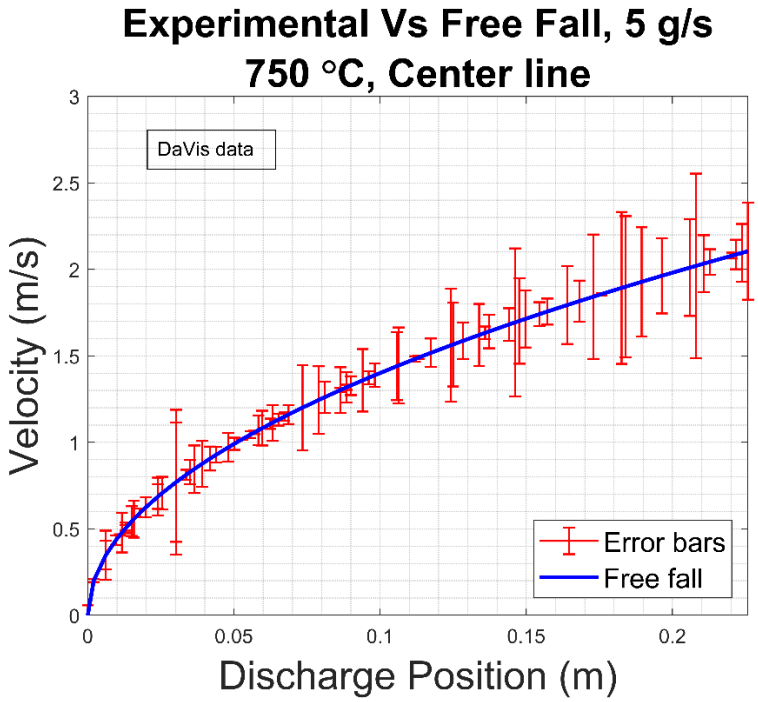

Figure 19: Discrepancies between the velocity profile from the center of the particle curtain and the expected free fall behavior at 750°C. DaVis analysis data.

Expanding more on this comparison between the two PIV packages and the expected behavior of the curtain of falling particles, nine cases were selected to realize a comparison at different flowrate, different temperatures, and different flow shapes. To alternate the shape of the curtain a wadge was added between the metallic and the top hopper, effectively splitting the flow into two curtains of falling particles. The orientation of the wedge was such that from the camera point of view the cross-sectional area of the curtain was unaffected.

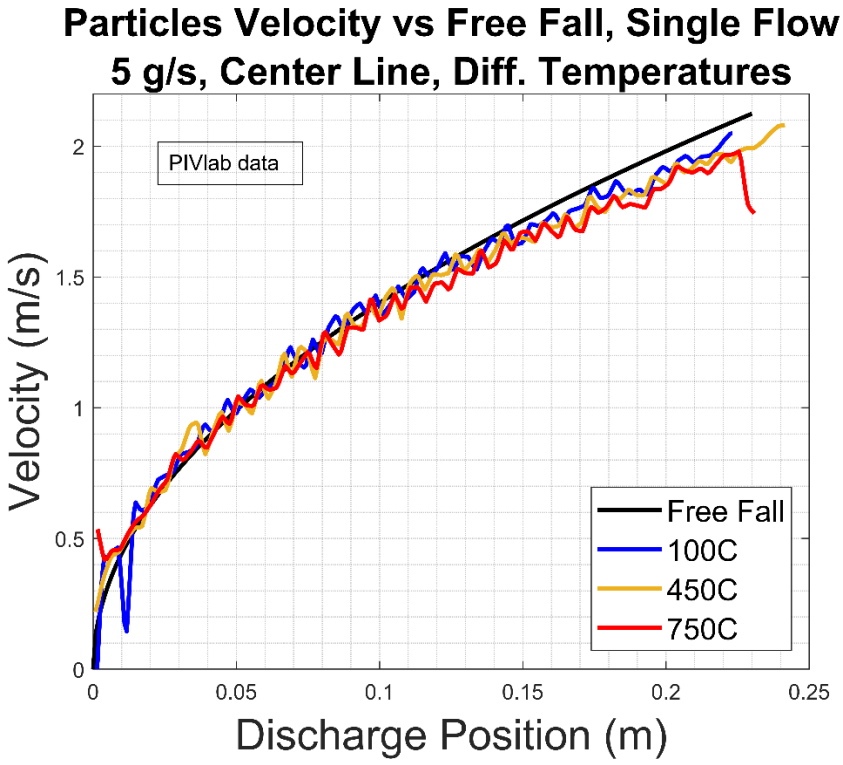

Figure 20: Center line velocity profiles at different temperatures with a single mass flowrate of 5 g/s. PIVlab used for the PIV analysis.

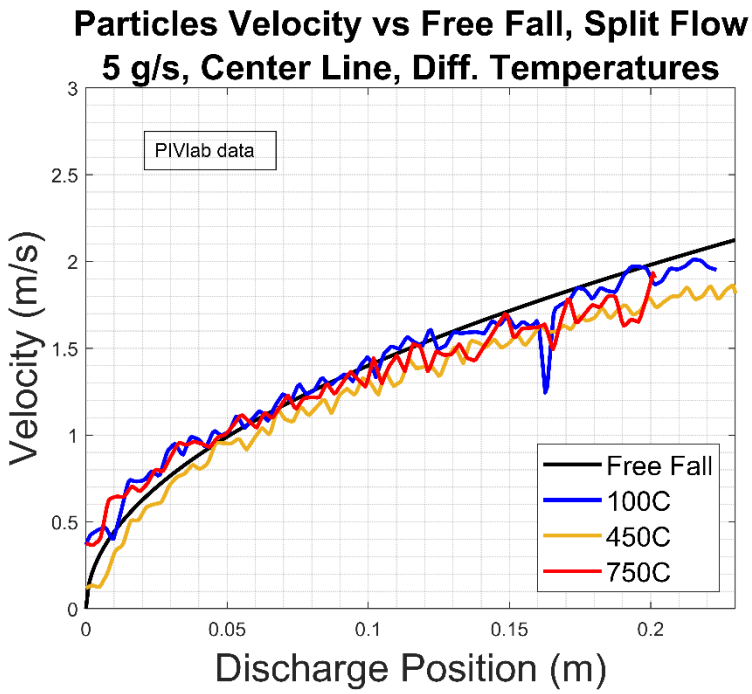

Figure 21: Center line velocity profiles at different temperatures with a split mass flowrate of 5 g/s. PIVlab used for the PIV analysis.

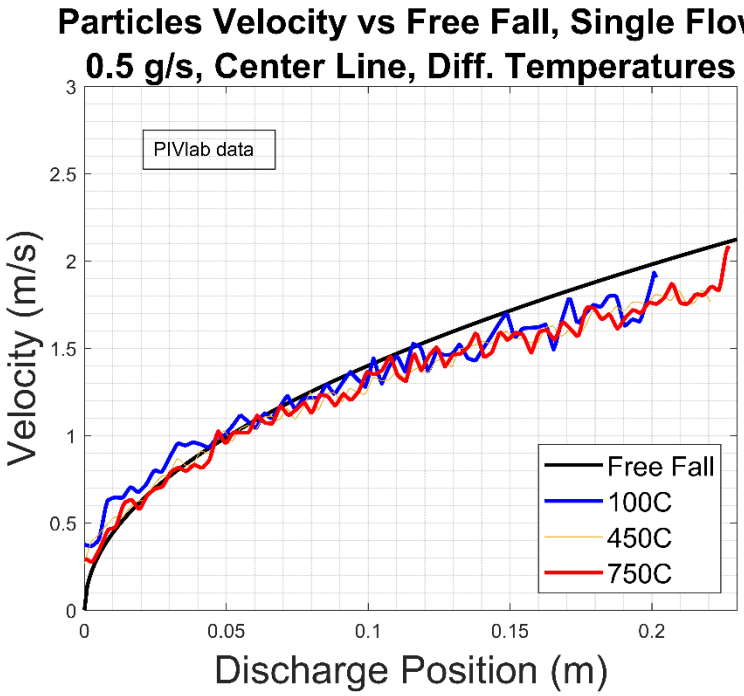

Figure 22: Center line velocity profiles at different temperatures with a single mass flowrate of 0.5 g/s. PIVlab used for the PIV analysis.

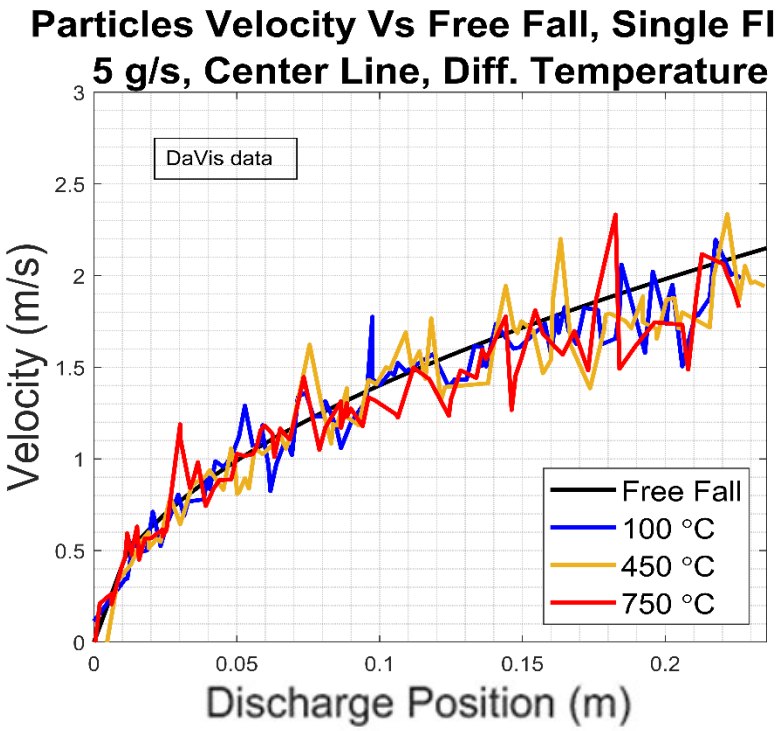

Figure 23: Center line velocity profiles at different temperatures with a single mass flowrate of 5 g/s. DaVis used for the PIV analysis.

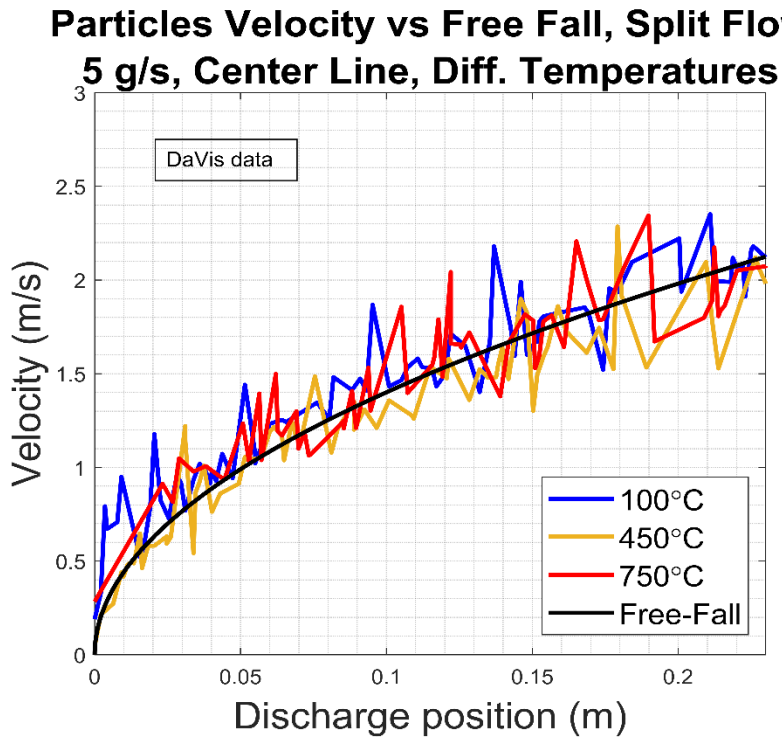

Figure 24: Center line velocity profiles at different temperatures with a split mass flowrate of 5 g/s. DaVis used for the PIV analysis.

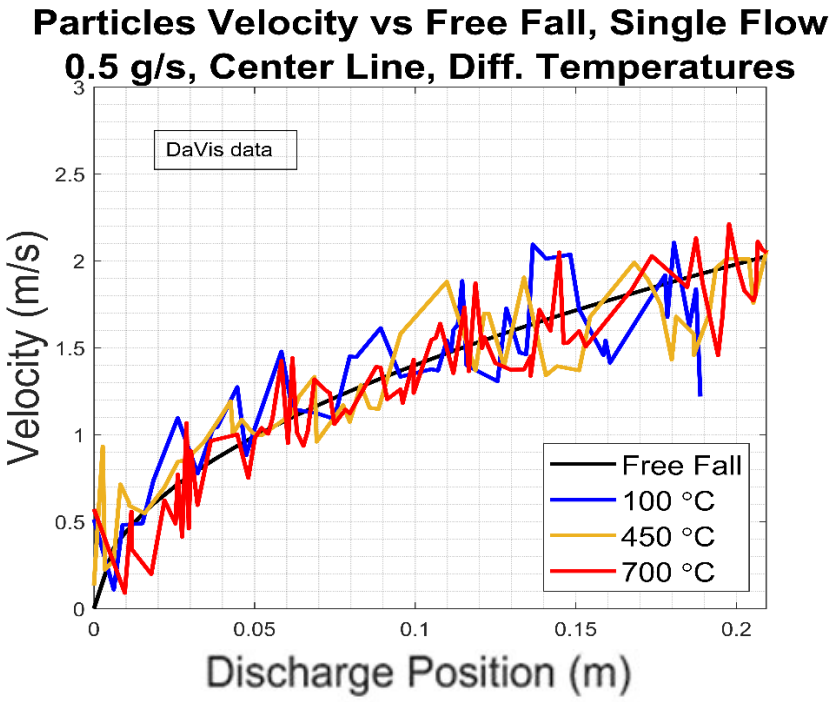

Figure 25: Center line velocity profiles at different temperatures with a single mass flowrate of 0.5 g/s. DaVis used for the PIV analysis.

Figures 20-25 illustrate two key factors; 1) Both, PIVlab and DaVis show velocities that are corresponding to what was expected to for a free fall particles curtain. In this way, demonstrating that it is possible to extract bulk velocities from sequences of thermograms despite the particles being of a smaller diameter than that of the pixel's size of the high-speed IR camera. 2) the behavior of the curtain can be affected to some degree by the temperature of the particle, and that the mass flowrate also has an impact on the behavior of curtain. Higher temperatures along with low mass flowrate result on a decrease in velocity at the bottom of the curtain. This can be attributed to an increased drag effect on the particles as due to their velocities increasing and subsequently separating them one from anther allowing for more air to enter the curtain. The air entering the curtain increases the drag experienced by the particles, and as this air gets heated up

its density changes making it more buoyant, thus moving on an opposing direction to that of the particles flow, further increasing the drag effect.

Moreover, the experiments conducted at the UNM facilities demonstrated that it is possible to obtain mass flow rates from implementing Eqn. 10 ($\dot{m}_p = -\frac{2}{3} D_p \rho_p \, ln(1-\omega) \, w_c V_b$) as demonstrated by Ortega et al where the use of the free fall velocity model for the curtain of particles was implemented. The opacity from the visual images was also computed, to determine the mass flow rate of the curtain. Results that were compared against the measured mass flow rate of the conducted experiments as shown on Figure 26 where measured mass flow rate of 5.2 g/s is compared to the calculated mass flow rate obtained implementing Eq. 10. [13] More examples along with a more elaborated description on how the mass flow rate was calculated can be found on the work presented by Ortega et al [13]

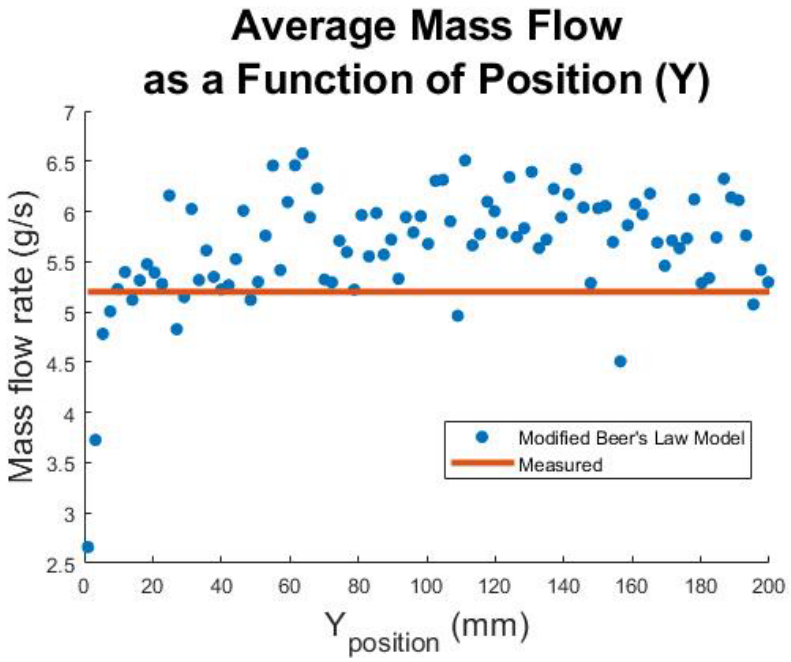

Figure 26: Comparison of Mass Flow Rate estimated using Eq. 10 and Measured Mass Flow Rate. Measured Mass Flow rate of 5.2 g/s [12], [13]

4.3 On-Sun Testing at the National Solar Thermal Testing Facility

Based on the results obtained at the UNM facilities the team concluded that the methodology was ready to advance into the next phase of the project. It was implemented into the evaluation of advective losses at the Falling Particle Receiver located in Sandia National Laboratory, more specifically at the NSTTF.

4.3.1 Field Set Up

Like at the UNM Solar Simulator facilities, the cameras were situated five meters apart from the point of interest, in this case, five meters apart from the center of the aperture of the falling particle receiver. The IR camera along with the visible camera were placed inside a protective enclosure to prevent any damage for the particles being expelled out of the FPR aperture. The enclosure is equipped with a quartz window and an IR window to protect the camera lenses as can be seen in Fig. 26.

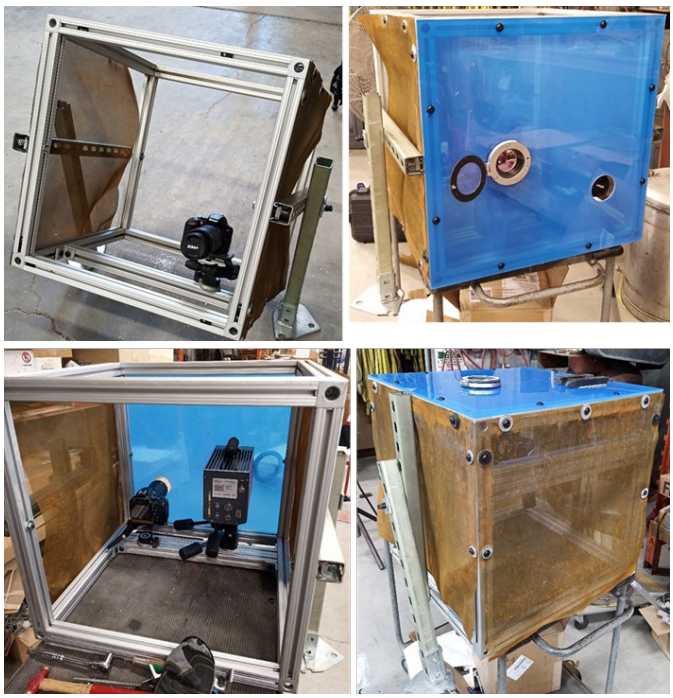

Figure 27: Enclosure built to protect and mount the IR camera as well as the visual camera[7].

The enclosure shown on Fig. 26 was then mounted into a testing stand specifically design for the purpose of allocating the cameras at the desired distance from the center of the FPR aperture.

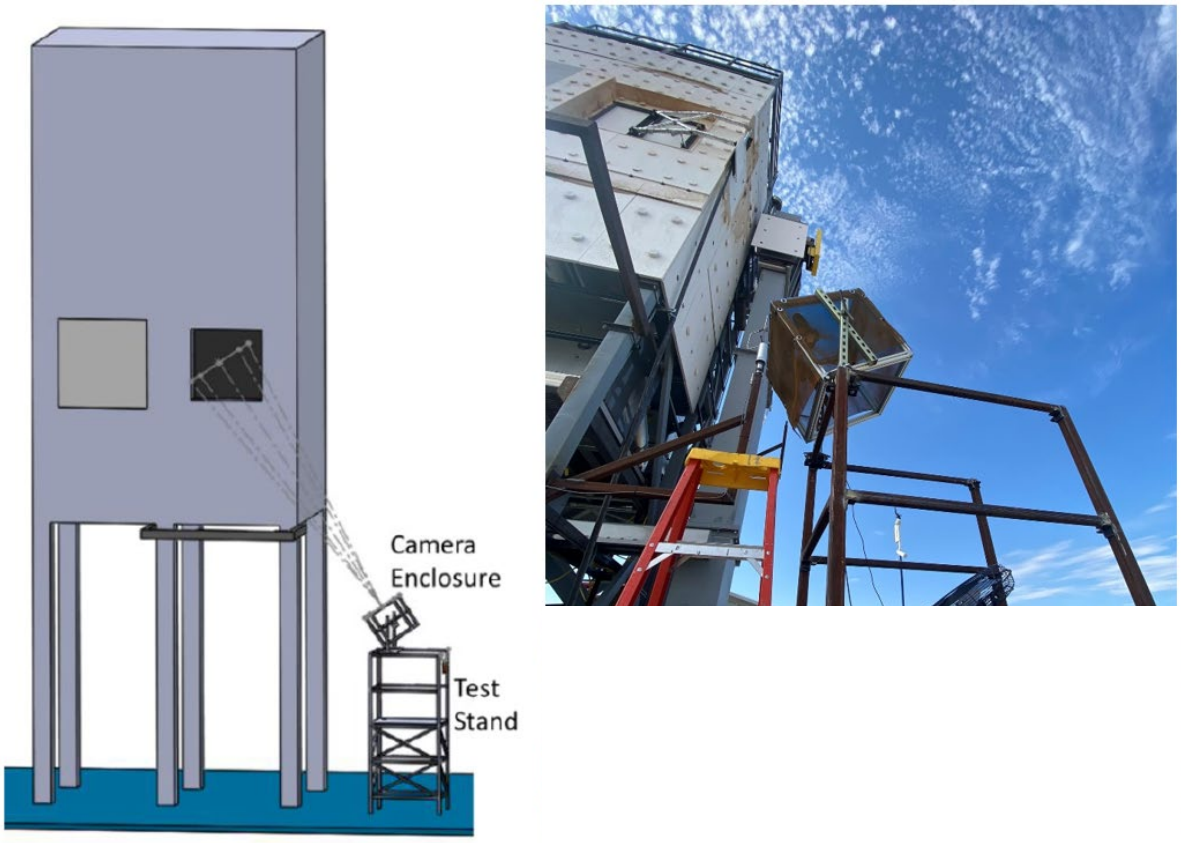

Figure 28: To the left, CAD Design of cameras test stand with enclosure mounted with respect to the FPR [7]. To the rigtht, a picture of the builed camaeras test stand.

The next step was to determine the most suitable location for the data acquisition (DAQ) system in order to maintain the used electronics within the temperature operational range to avoid having any inconsistencies and errors during the data collection process. After completing an assessment to determine the location of the DAQ system, the team concluded that the best location for the system was the room located under the FPR. During the testing campaign, the FPR was

located at the 280 level in the Solar Tower. Fig. 28 shows a diagram schematic displaying the wiring arrangement and location of the cameras and the DAQ system.

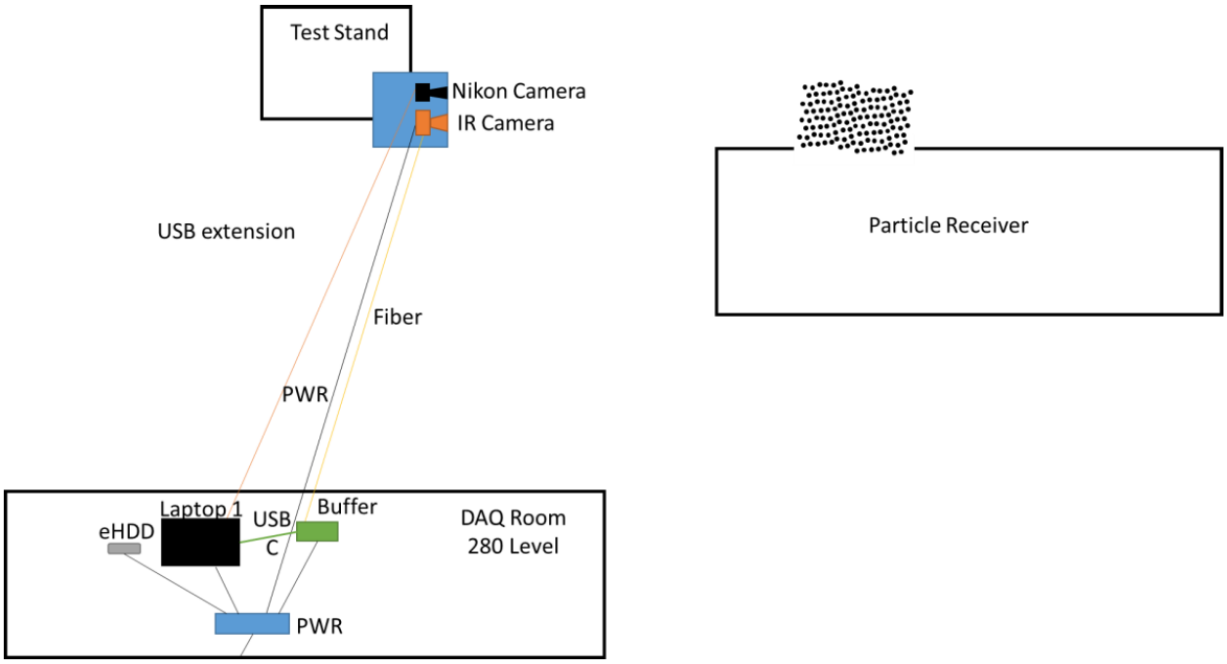

Figure 29: Wiring diagrams and positioning of the cameras with respect to the particle receiver on top of the tower. The DAQ room is located at the 280 level (20 ft below the roof of the tower).[11], [12]

4.3.2 Field Tests and Results

Multiple tests were conducted at the Sandia NSTTF through which about 20 Terabytes of data were acquired. For the test conducted at the NSTTF the data acquisition process deferred from the process at the UNM facilities by changing the sampling rate. While at the UNM solar simulator the IR camera was used to capture lapse of time of about 1 second with a sampling rate of 300 Hz, at the NSTTF the IR camera sampling rate was kept the same sampling rate but, in this case, it was used to capture lapses of time of 2 minutes every 2 minutes, resulting in a total of 36,000 thermograms per every 2 minutes of capturing data. Likewise, the sampling rate of the visual camera was kept close to that of the experiments conducted at the UNM facilities, but with an operational time of 2 minutes. Resulting on about 12 GB of captured data per measurement, thus

the immense amount of date obtained[11]. One of the reasons for increasing the amount of time on the recording is that the plumes of particles are expelled out of the aperture on a random basis, therefore a longer recording time increases our chances to capture those plumes.

While testing and analyzing the data being obtained at during the operation of the FPR it was noted that there were multiple entities being capture by the cameras other than the particles of interest, as can be seen on Fig. 28.

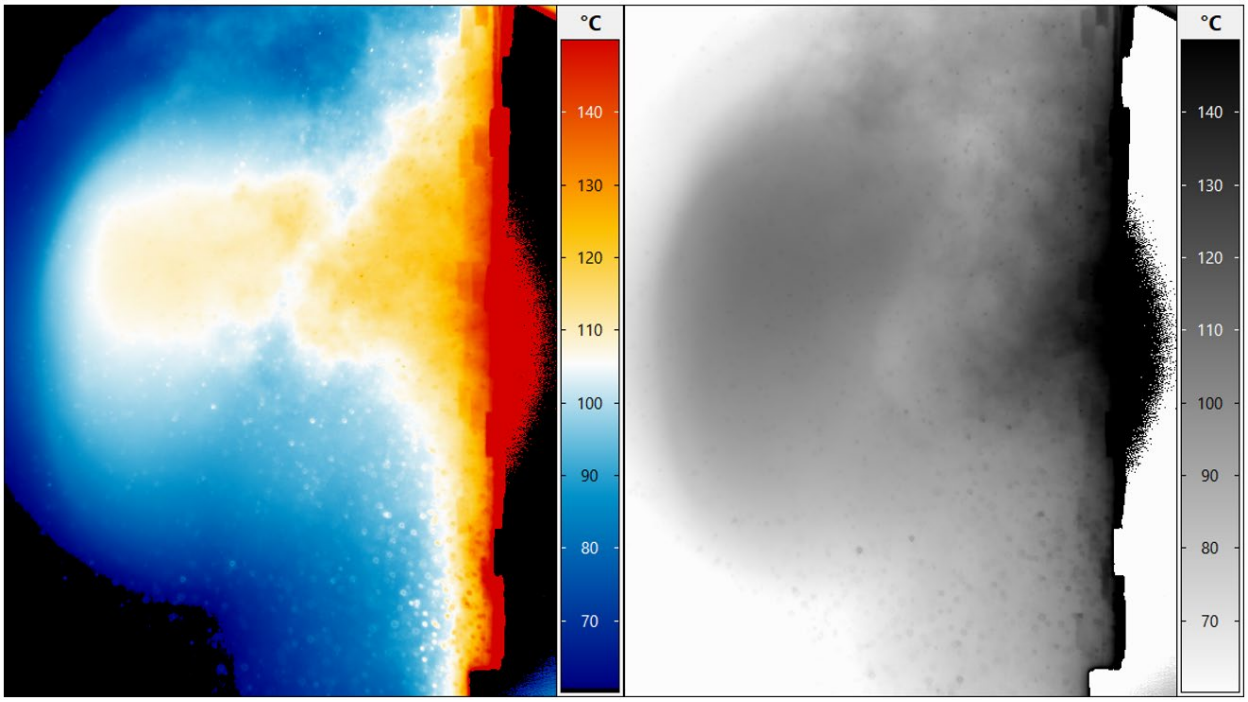

Figure 30: Thermograms obtained during testing at the NSTTF. To the right is thermogram on the RGB color scale. To the left the thermogram with the gray scale.[11]

Due to these other entities present on the thermogram there was a concern regarding the effect that it would have regarding the velocity vectors and other properties of the flow obtained through image processing. On first instance, a small comparison study was conducted to determine if the color scale would have considerable impact when extracting the velocity vector field. For

this study, the same set of thermograms was extracted twice using different color scales (i.e., gray and RGB). Then, the sets went through PIVlab to extract the velocity vector fields for later comparison. Fig. 29 shows the average velocity vector field obtained from the set extracted at the different color scales. The selected set shows plume of particle being ejected out of the FPR aperture, thus making it a notable set to be used for the comparison study. This set is composed by a total of 781 thermograms shot with a frequency of 300Hz, covering a time lapse of about 2.3 seconds.

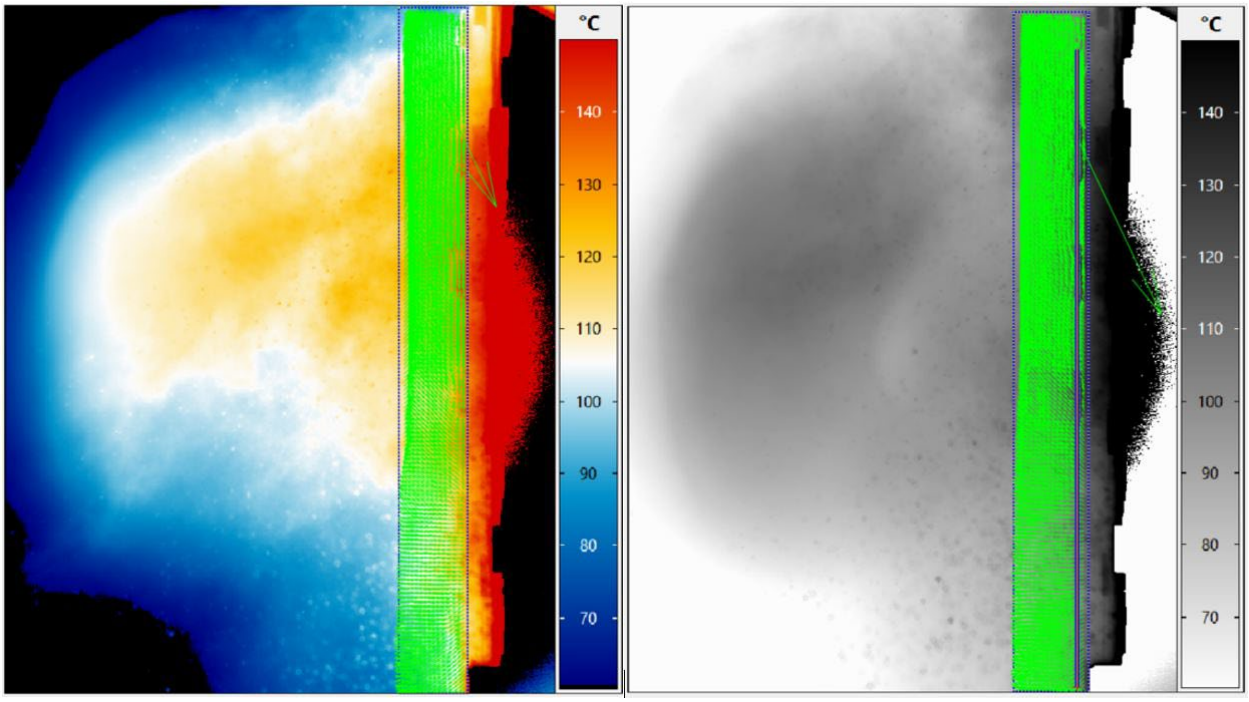

Figure 31:Average velocity vector field extracted from a .3 second time lapse in the two different color scales (RGB to the right, Gray to the left)

As the goal is to calculate the egress rate of particle out of the FPR aperture, the comparison was focused on the velocity of the particles perpendicular to the aperture and the closest possible to the aperture. For this comparison, the velocities were extracted using a polyline located to the

right of the ROI as it is the closest location to the aperture. Multiple frames were selected for this comparison as to determine the effects of the color scale has the calculated velocity vector fields.

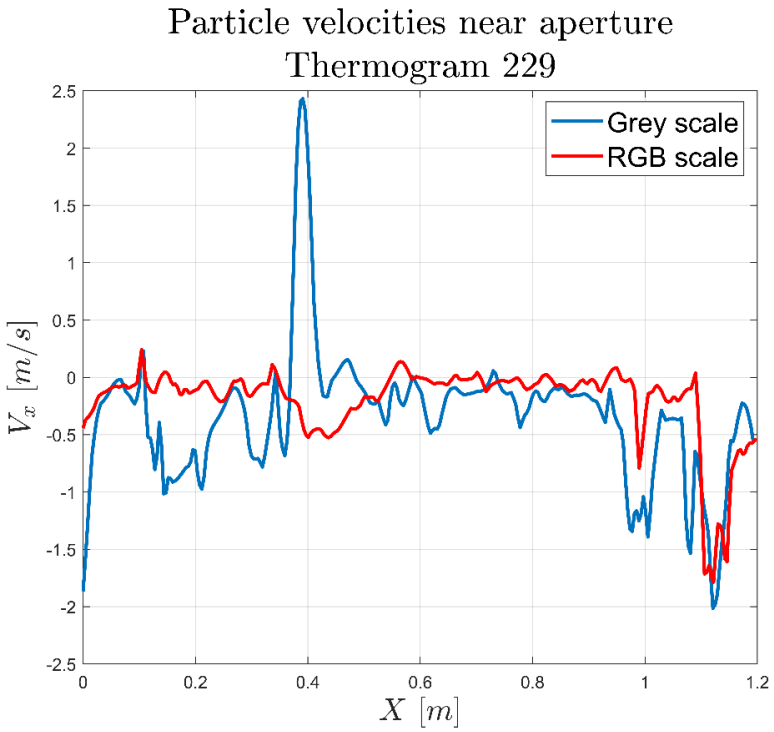

Figure 32: Comparison of velocities obtained from PIV analysis on the RGB and Gray scale thermograms. Thermogram 229.

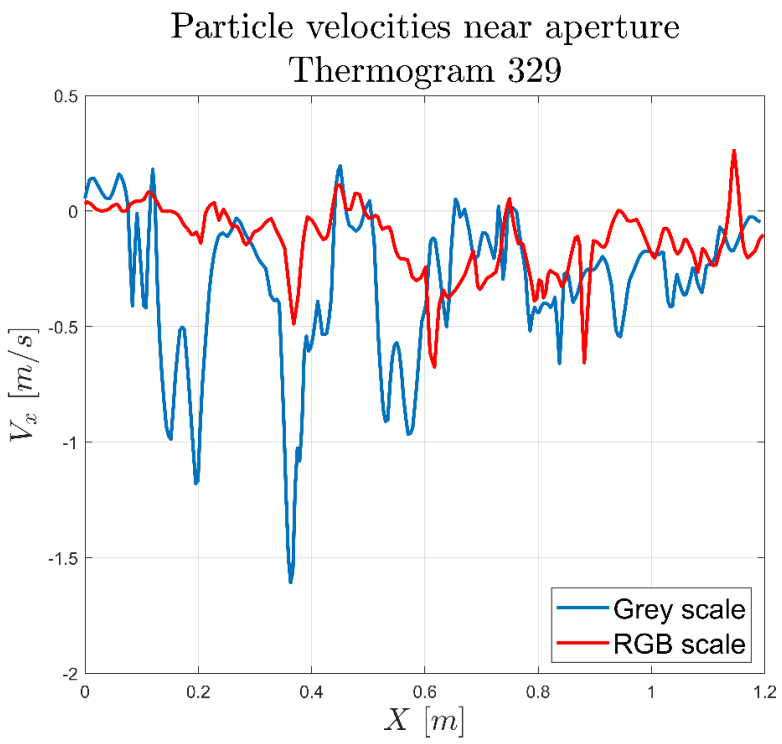

Figure 33: Comparison of velocities obtained from PIV analysis on the RGB and Gray scale thermograms. Thermogram 329.

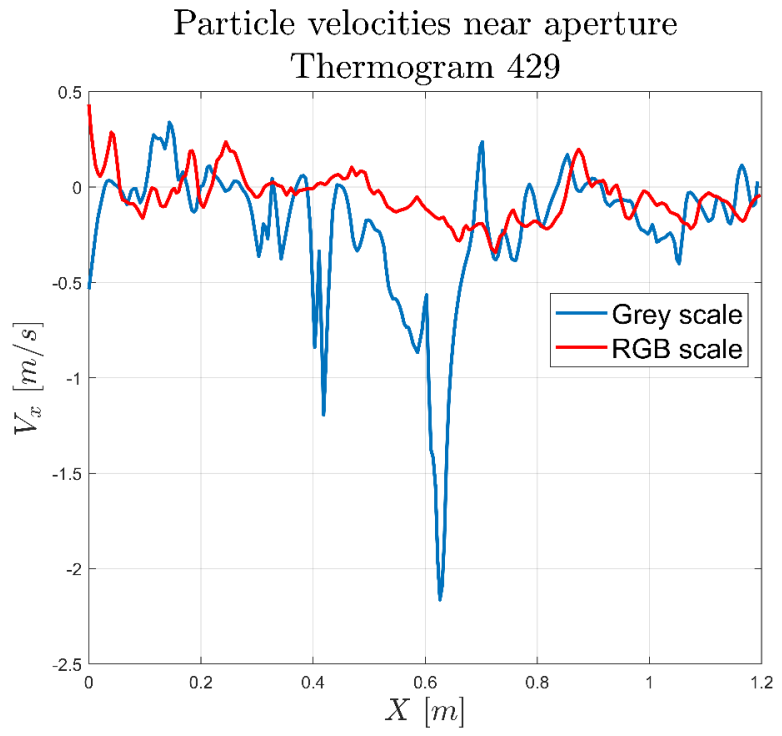

Figure 34: Comparison of velocities obtained from PIV analysis on the RGB and Gray scale thermograms. Thermogram 429.

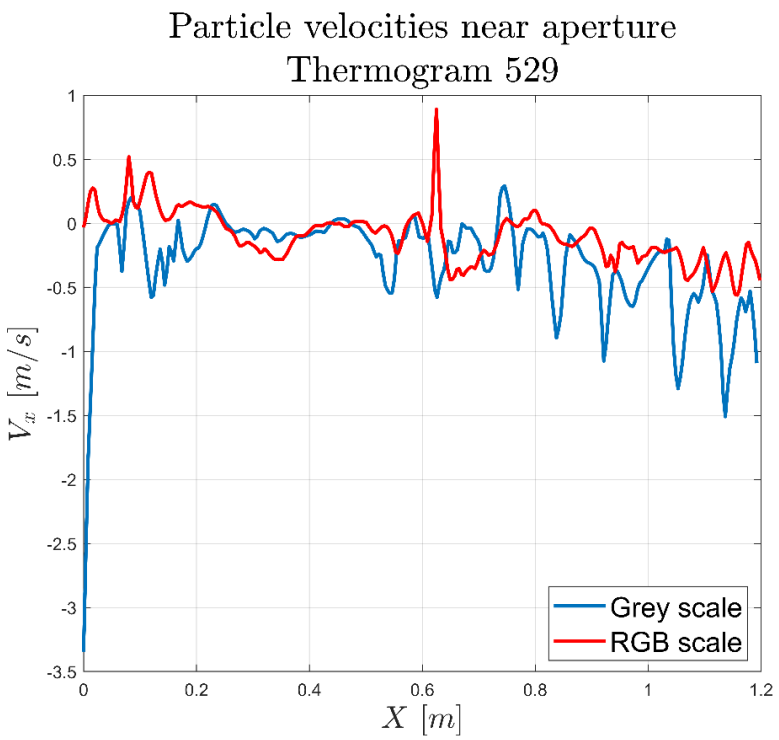

Figure 35: Comparison of velocities obtained from PIV analysis on the RGB and Gray scale thermograms. Thermogram 529.

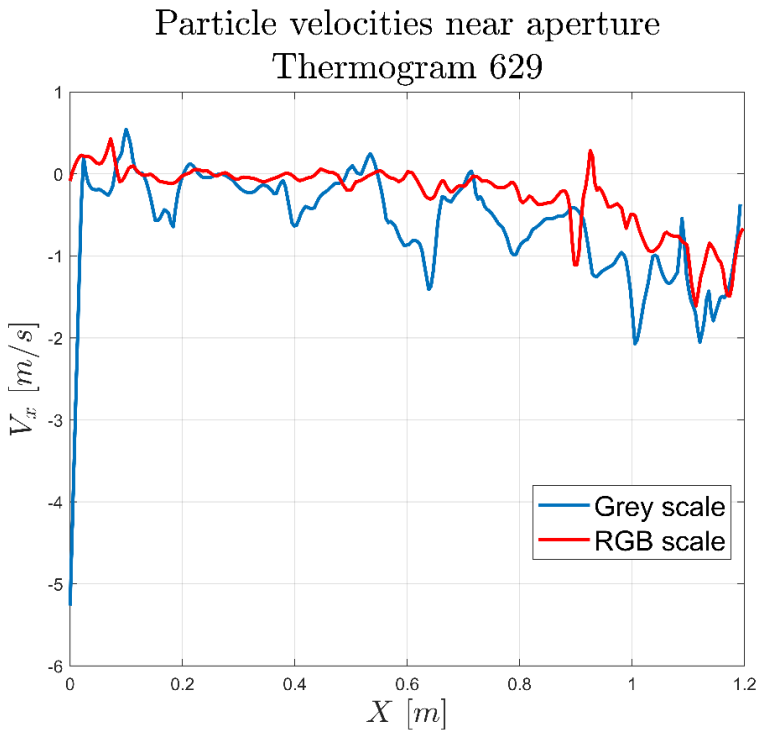

Figure 36: Comparison of velocities obtained from PIV analysis on the RGB and Gray scale thermograms. Thermogram 629.

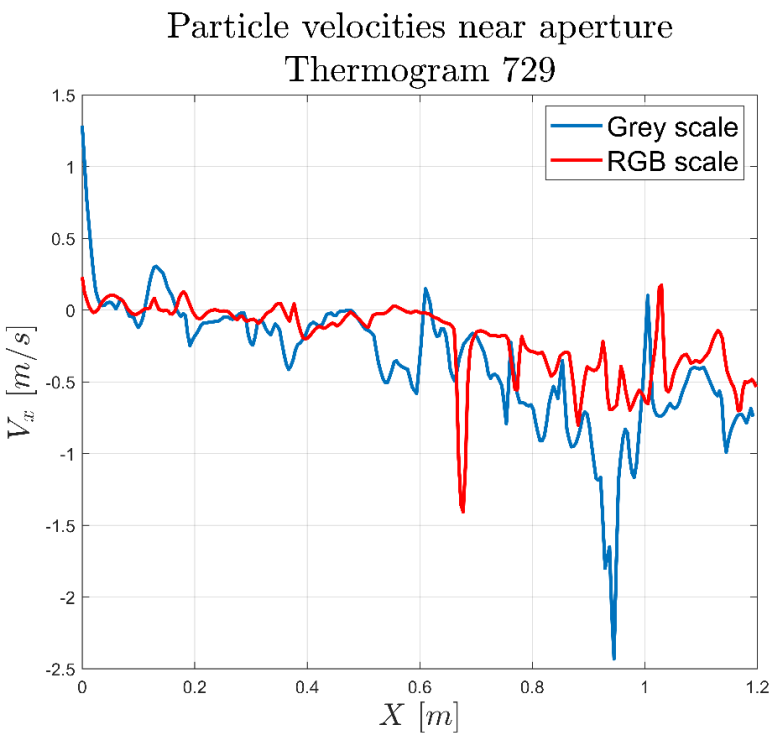

Figure 37: Comparison of velocities obtained from PIV analysis on the RGB and Gray scale thermograms. Thermogram 729.

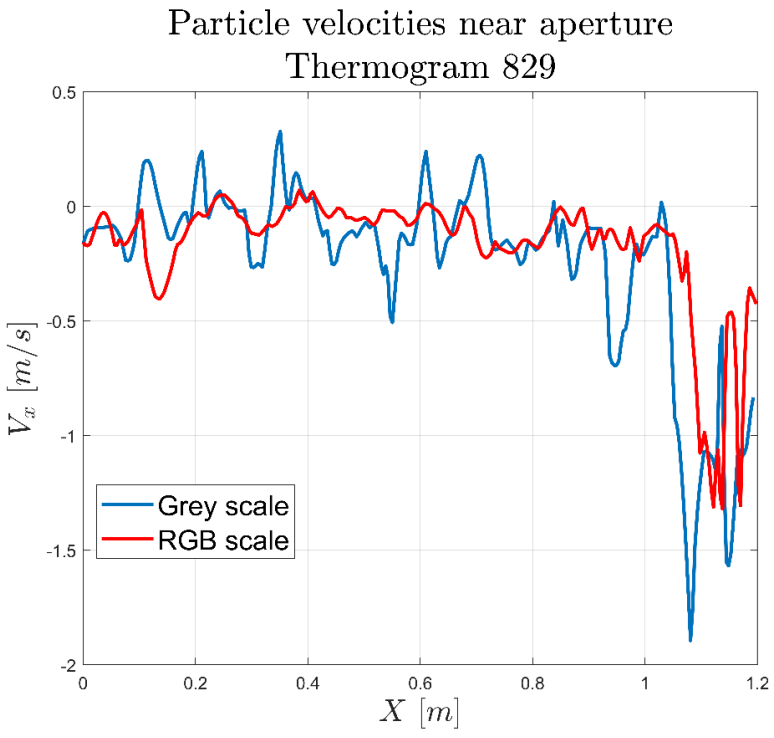

Figure 38: Comparison of velocities obtained from PIV analysis on the RGB and Gray scale thermograms. Thermogram 829.

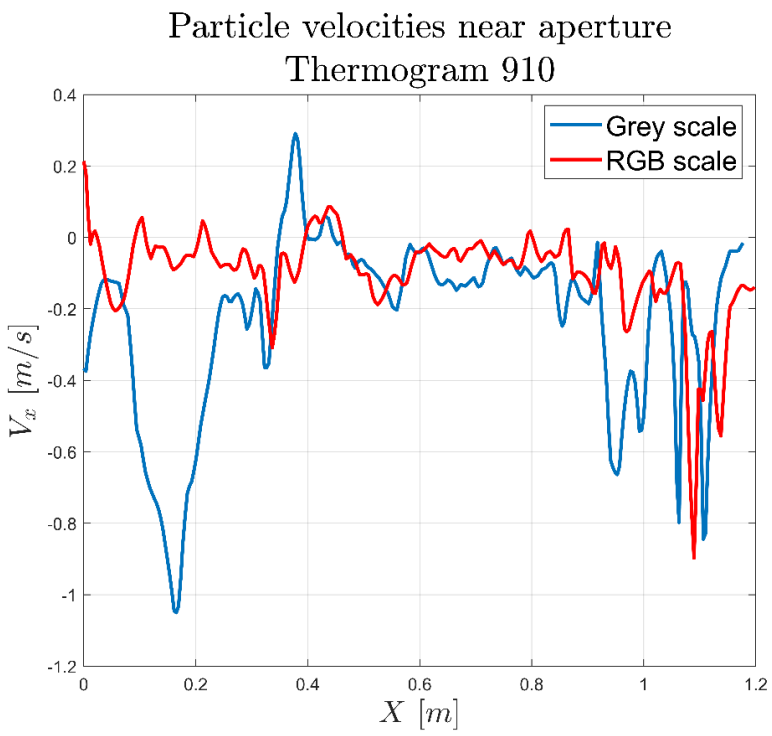

Figure 39: Comparison of velocities obtained from PIV analysis on the RGB and Gray scale thermograms. Thermogram 910.

As it can been seen on the above figures, the calculated velocity vectors using PIVlab tend to follow the same behavior along the polyline with the exception of some "randomly" located peaks where the velocities spike to higher magnitudes. This is believed to be an effect related to the noise precent on the thermograms background (dust, particles out of the focal range). In an effort to reduce the effect of the noise and to increase the fidelity of the measurements it was deemed necessary to remove as much of the present noise/dust as this cannot just affect the velocity measurements but the temperatures readings [7], [12], [31], [33]. To remove the presence of dust from both, the visual images and the thermograms a median filter was applied to remove the outlier pixels (i.e., pixels containing particles) leaving only behind the background and the dust. Then the filtered-out images with no visible signs of outliners are used by the algorithm to find the pixels

containing an intensity higher than that of the background with dust, so the algorithm yields a new image with particles only. Then, to evaluate how efficiently these pixels were being removed from the original images by the median filter, the structural similarity index measure (SSIM) was implemented to measure the perceptual difference between the original (RAW image and thermogram) and the filtered images. For the visual images, a matrix size of approximately 90x90 was used as a filter to converge the images to be 90% similar as a result of filtering out the outliners. Fig. 39. [11], [12]

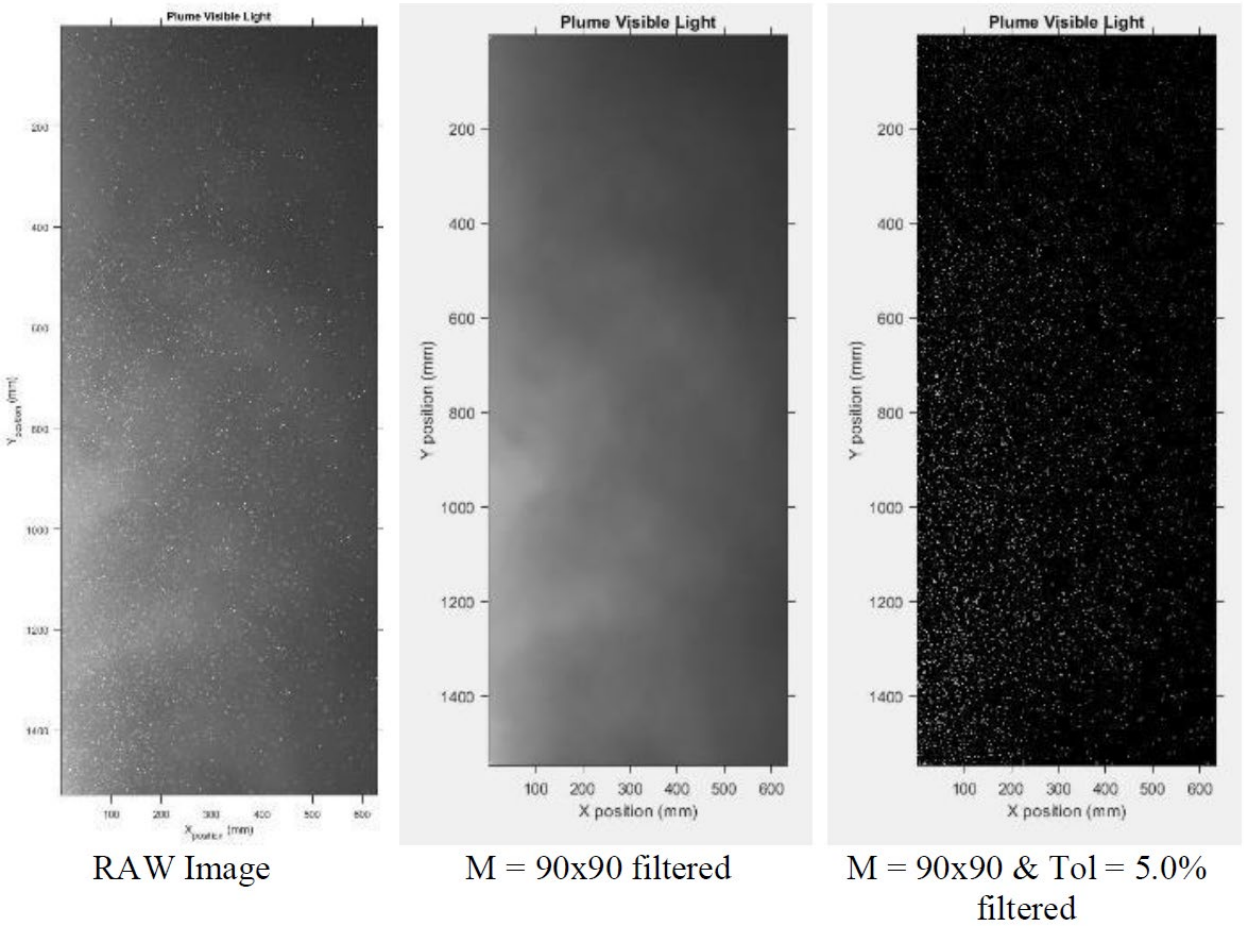

RAW Image | M = 90x90 filtered | M = 90x90 & Tol = 5.0% filtered

Figure 40:Original raw image (left). Resulting filtered image without particles (center). Final filtered image with particles only from the original RAW image (right).[11], [12]

As for the thermograms, the resulting images showed that a matrix of approximately 25x25 in size will sufficiently eliminate all the outliners as shown in Fig. 40. [11], [12]

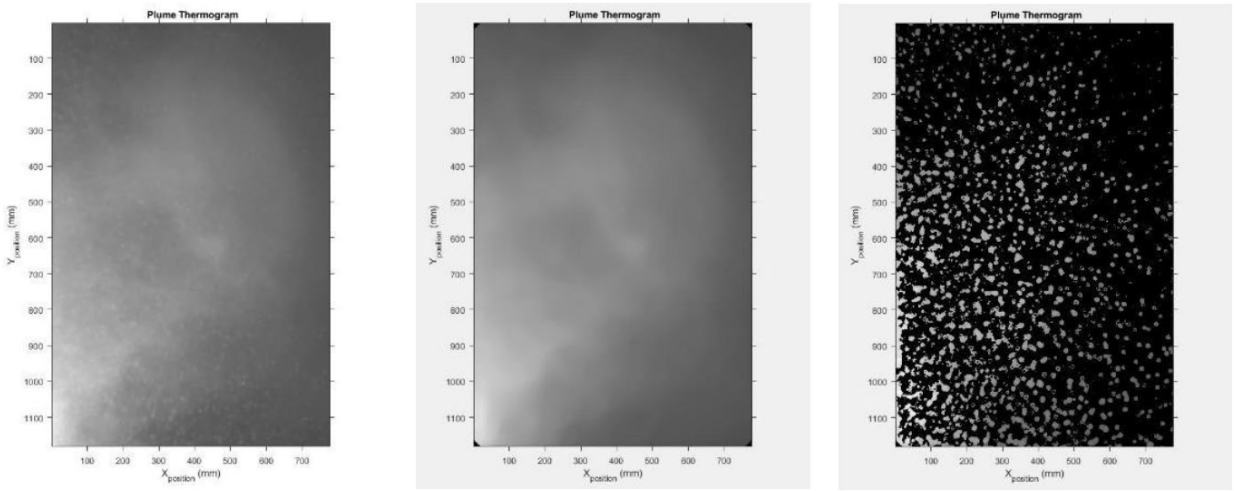

RAW Thermogram | M = 25x25 filtered | M = 25x25 & Tol = 1.5% Filtered

Figure 41:Original raw thermogram (left). Resulting filtered thermograms without particles (center). Final filtered thermograms with particles only from the original RAW thermogram (right).[11], [12]

Furthermore, the thermogram and visual image filtering process mentioned above was introduced to the main MATLAB script to improve the fidelity of the process. This was done while the source script for PIVlab was modified to be used as a simplified MATLAB function that can be ran from the script in conjunction with the rest of the main MATLAB script developed by Dr. Ortega [12]. To transform the source code into a simple function easy to apply on the main MATLAB script it was necessary to identify the necessary inputs required for the PIVlab run and to output the desired information. The identified inputs here used included the source directory for the images being analyzed, the pixel to mm scale, and the names of the files that were being analyzed. Then the function was set to provide three outputs: the velocity perpendicular to the FPR aperture, along with the corresponding x, and y location for such velocity. Thus, enabling the team to obtain the particle bulk velocities across the FPR aperture as seen in Fig. 41 [11], [12].

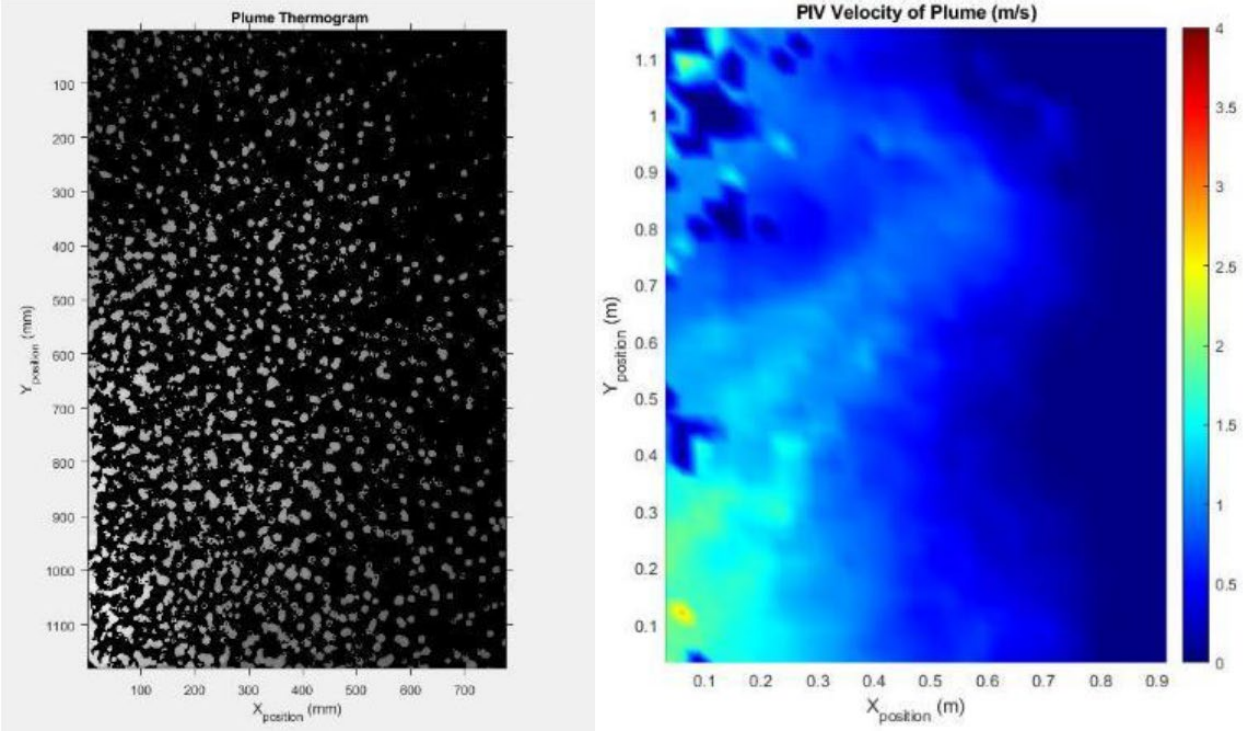

Figure 42: To the left one of the 10 thermograms used on the PIVlab analysis. To the right the velocity field map showing the horizontal component of the bulk velocities of the particles plume, which can be used to estimate the average X-velocity [11], [12].

Now being able to obtain both the velocities and the representative opacities used to calculate the plume density and temperature it's time to calculate the egress rates and advective losses of the FPR. As previously mentioned, each 2-minute measurement is composed by 65 images and 36,000 thermograms. Therefore, the team decided that the best way to describe the behavior of the system was to assume that for each visual image captured within the 2 minutes of data collection the conditions hold constant as it is the temporal resolution available with DAQ system implemented. The bulk velocity is equal to that of the average velocity obtained from the first 10 thermograms of the 554 thermogram sequence corresponding to each visual image capture [11], [12]. Implementing these considerations/assumptions, then the average particle egress rate

can be calculated following the work presented by Ortega et al [13], [34], while the respective particle and air heat losses can be calculated using Eq. 11 and Eq. 13 respectively [11]–[13].

Furthermore, the above mentioned can be observed in Figures 43 and 44 where the 65 corresponding temporal instances are shown. The first showing the average egress particle egress rate and the later the corresponding particle heat loss. This data was acquired on September 4th, 2020, at 10:59 AM. During the time encapsulated by the data collecting process, the receiver inlet and outlet temperatures were measured to be 362 °C and 408 °C respectively.

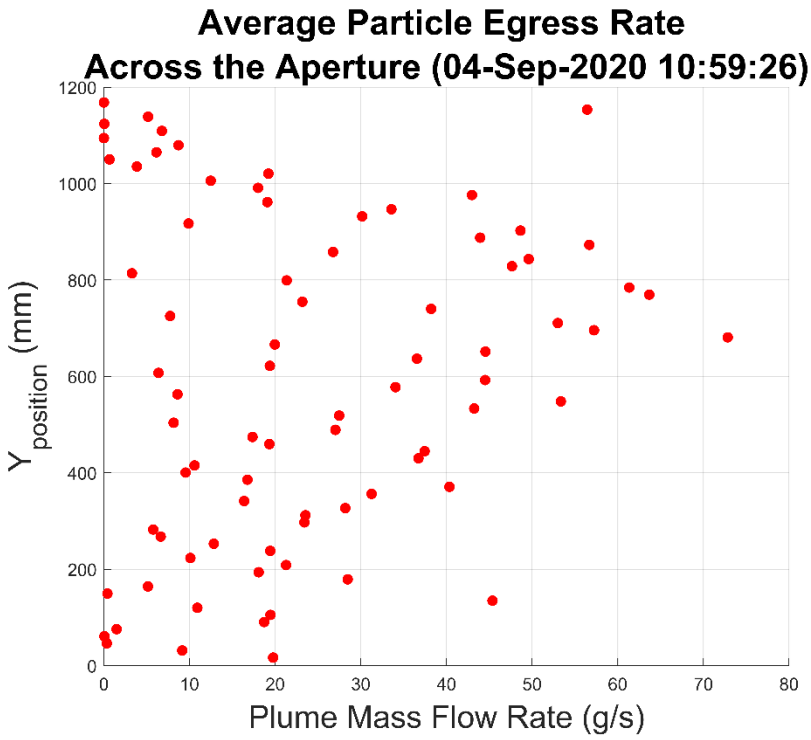

Figure 43: Average egress rates corresponding to each of the 65 images obtained for the 2 minutes of data collection. Third instantaneous particle egress rate of this set was calculated to be 23.9 g/s [11], [12].

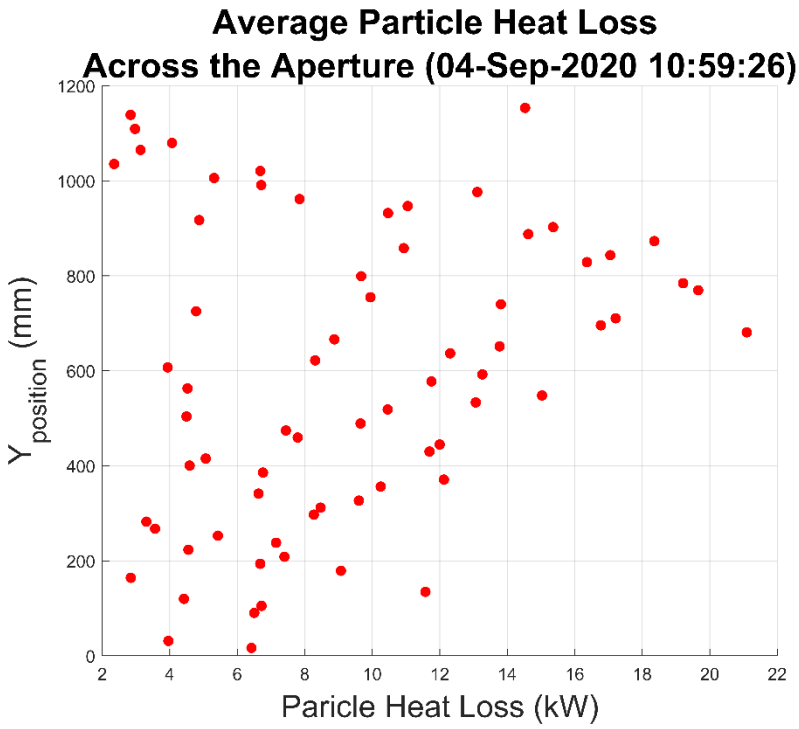

Figure 44:Average particle heat loss corresponding to each of the 65 images obtained for the 2 minutes of data collection. Third instantaneous particle heat rate of the set was calculated to be 9.3 kW [11], [12].

From the collected data it can be observed that calculated average temperature of particles being expelled from the FPR cavity is estimated to be about 403 °C, Fig. 45, which fall between the temperatures of the particles measured at the receiver inlet and outlet, 362 °C and 408 °C respectively[11], [12].

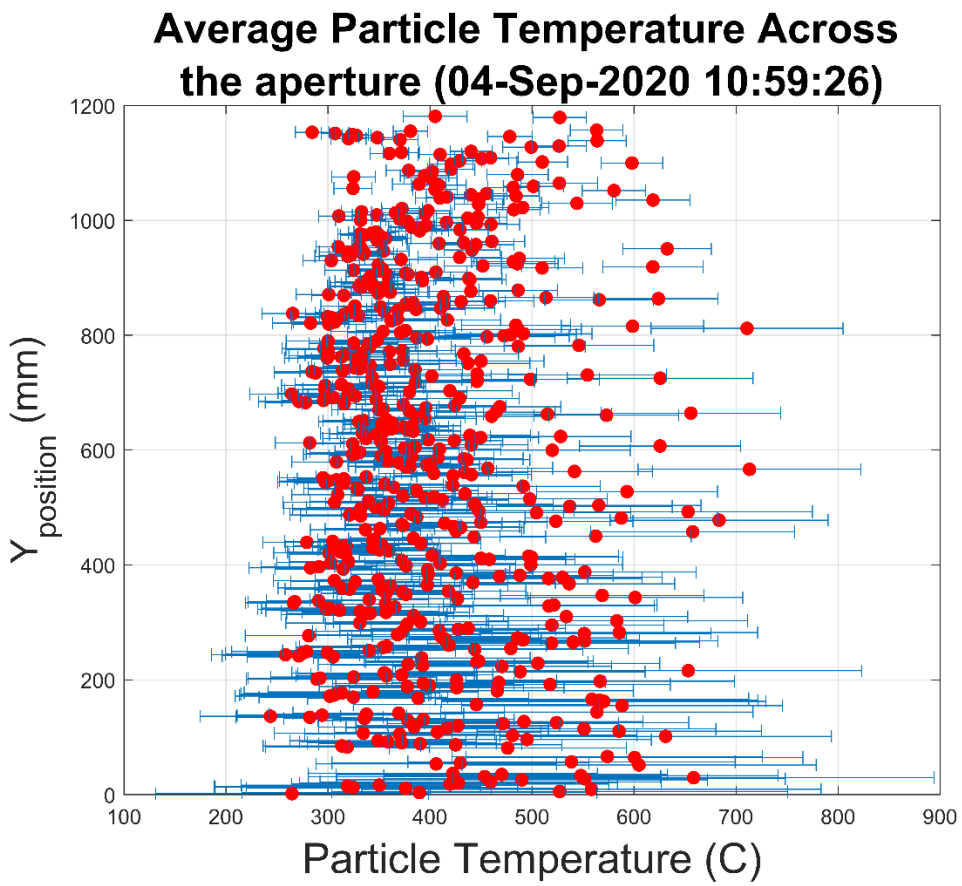

Figure 45: Estimated particle temperature using the methodology presented by Ortega et al. Calculated average particle temperature of 402.7 °C [11], [12].

Additionally, total average advective losses for this data set can be estimated to be 49.7 kW[11], [12]. As there are a total of 65 captures for the entire 2-minute data set, a time series plot can be generated with the average values of each instantaneous particle egress rate, as well as the corresponding instantaneous plume heat loss, as shown in Figure 46.

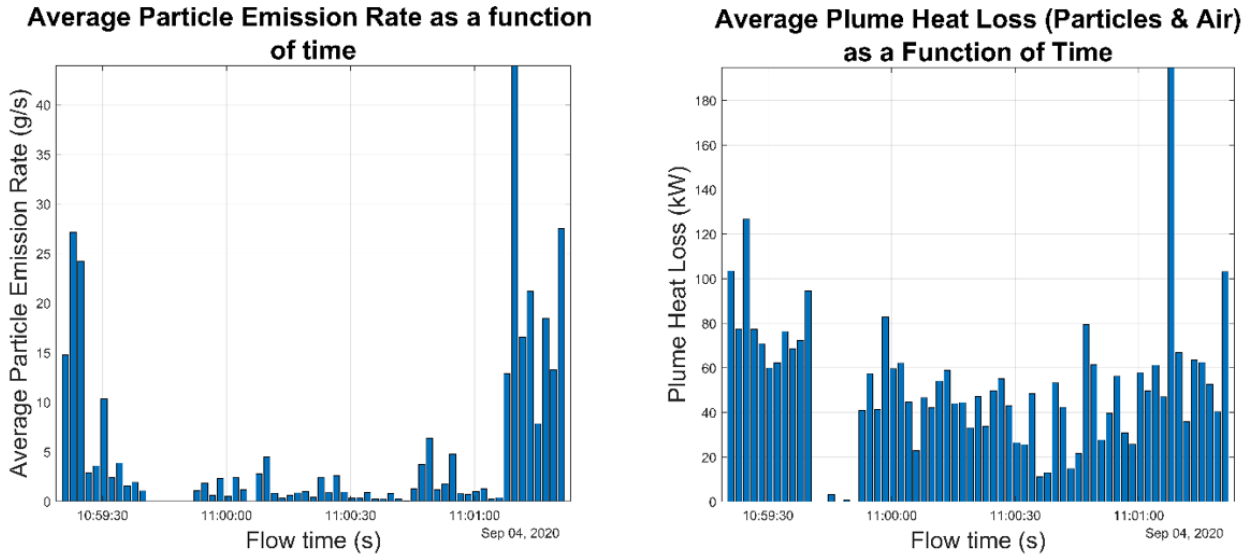

Figure 46:Left: Time series plots for particle egress rate during the 2 minutes of data collected, totaling about 0.63 kg. Right: Time series plots of average advective heat loss (i.e., particles and air within the plume) with an estimated total loss of 49.7 kW [11], [12].

As sanity check to ensure that the advective losses here presented are within reason one can implement the finding shown by Mills and Ho [35], where through fluid dynamics simulations they showed that approximately 70% of the total thermal losses from the FPR were due to advective/convective losses from the cavity. Meaning that the total heat losses from the receiver can be approximated using Equation 16.

$$\dot{Q}_T = \frac{\dot{Q}_A}{0.7} \tag{16}$$

Applying Eq. 16 to the obtained estimated advective losses yield an estimation of approximate 71 kW in total losses. Meaning that for an input power of 420 kW, the receiver efficiency can be estimated to be 83.1%, which closely agrees with those measurements at the receiver for the corresponding data recording time which ranged from 79% to 83% [11], [12].

Additionally, more cases like this were analyzed by Ortega et al where it was found that as the temperature increases some discrepancies began to appear. It is believed that for particle temperatures over 500 °C the radiative losses become much more dominant causing the particles to cooldown faster [11].

CHAPTER 5: CONCLUSION

As the demand for energy keeps growing innovative technologies are emerging to face this challenge. Concentrated Solar Power technologies have been in the raise during the last decades, and they have been shown to be promising technologies in the efforts for meeting the energy demands as well as for reducing dependency on fossil fuels. The Falling Particle Receiver at the National Solar Thermal Testing Facilities represents one of the lates advancements for CSP energy harvesting technologies. The FPR utilizes solid particles as the working Heat Transfer Fluid, and as the storage media for the CSP energy absorbed.

The FPR operates by generating a gravity-driven particle curtain that is exposed to the concentrated sun irradiation produced by a field of heliostats through an open cavity. However, during operation it has been noticed that random plume of particles from the particle curtain were being expelled out of the cavity resulting both particle inventory and heat losses from the system. The work here presented forms part of an effort to develop a methodology using a high-speed IR camera and a visual camara to characterize these plumes and thus estimate the advective losses of the system.

Moreover, the work here presented is focused toward the rolled played by applying Particle Image Velocimetry techniques with sets of thermograms form the high-speed IR camera to determine the velocity component required to calculate the egress rate of the particles from the FPR, Eq. 10. First, it was necessary to demonstrate that it was possible to obtain reliable velocity

reading from the high-speed thermograms through means of PIV techniques. To achieve this the team provided a validation by comparison between the MATLAB PIV toolbox, PIVlab, and the commercially available PIV software DaVis, along with a comparison to previous documented models of behavior for gravity-driven particle curtains [13], [15].

Additionally, during this process the team also learned how the mass flow rate and particle temperature influence gravity-driven particle curtains. It was noted that as the particle temperate increased and the mass flow rated decreased, an increased drag effect was observed. The team determined that with smaller mass flow rates the decreased curtain density resulted in more air flow between particles pulling them apart resulting on particles experiencing the effects of drag. It was also noted that the effects of drag were aggravated with low mass flow at high temperatures (>500°C). The team concluded that this effect could be explained by the high-temperature particles heating up the air entering the curtain having two consequences as result. The first consequence is a slight increase of viscosity of the air surrounding the particles. The second consequence is a buoyant effect of the air, where the heated air moves in an opposite direction of that of the curtain flow. As a result, the UNM lab-scale testing campaign proved, over a controlled environment, that it is possible to utilize PIV techniques on the high-speed thermogram sets to determine the bulk velocities of the particles and to use such velocities to determine the particle mass flow rate [12], [13], [15], [16]. This proves that part of the research's novelty was successfully completed.

Furthermore, after showing that the methodology developed worked at the UNM controlled lab facilities, a real scale, on-sun test campaign at the NSTTF was conducted to assess the methodology over a less controlled environment and with the real-world operations conditions of the FPR. AS a result of this test campaign some modification and extra processing steps were integrated to the methodology as to account for the factors present at the FPR that were not present

at the lab-scale. Adaptations were included to the experimental set up to protect the used cameras and avoid any damage to the DAQ systems, as well as to ensure the DAQ was kept at operating temperatures to avoid suffering any inconsistencies and errors during operation. This testing campaign yielded promising results for the developed methodology, providing advective losses estimations. These estimations agreed in most of the presented cases with the efficiency measurements of the FPR, except for some high temperature cases where the advective losses where underestimated. For the cases in which this was observed, the team concluded that the discrepancy can be attributed to a faster cooling rate present on the high-temperature particles egressing from the FPR aperture. This is due to the radiative heat loss that becomes more dominant at temperatures above the 500 °C [11], [12], [14], [16].

Based on the results of our research, I consider that one way to increase the fidelity and precision of the developed methodology would be to pair the high-speed IR camera with a high-speed visual camera with similar capabilities as to have a one-to-one comparison between the thermograms and the visual images. For future work, it could also be considered to implement the use of more cameras from different angles in an effort to characterize the 3D properties of the particle plumes leaving the FPR cavity. These additions could potentially improve the characterization of the advective losses of the system that can lead to design improvements for the FPR.

References

[1] D. L. Chandler, “Shining brightly | MIT News | Massachusetts Institute of Technology,” *MIT News Office*, 2011. https://news.mit.edu/2011/energy-scale-part3-1026 (accessed May 12, 2022).

[2] L. H. Yang, J. De Liang, C. Y. Hsu, T. H. Yang, and S. L. Chen, “Enhanced efficiency of photovoltaic panels by integrating a spray cooling system with shallow geothermal energy heat exchanger,” *Renew. Energy*, vol. 134, pp. 970–981, 2019, doi: 10.1016/j.renene.2018.11.089.

[3] C. K. Ho, “A review of high-temperature particle receivers for concentrating solar power,” *Appl. Therm. Eng.*, vol. 109, pp. 958–969, 2016, doi: 10.1016/j.applthermaleng.2016.04.103.

[4] C. K. Ho, “Advances in central receivers for concentrating solar applications,” *Sol. Energy*, vol. 152, pp. 38–56, 2017, doi: 10.1016/j.solener.2017.03.048.

[5] N. P. Siegel, C. K. Ho, S. S. Khalsa, and G. J. Kolb, “Development and evaluation of a prototype solid particle receiver: On-sun testing and model validation,” *J. Sol. Energy Eng. Trans. ASME*, vol. 132, no. 2, pp. 0210081–0210088, 2010, doi: 10.1115/1.4001146.

[6] C. Ho *et al.*, “Technology advancements for next generation falling particle receivers,” *Energy Procedia*, vol. 49, pp. 398–407, 2014, doi: 10.1016/j.egypro.2014.03.043.

[7] J. D. Ortega and C. K. Ho, “A NON-INTRUSIVE PARTICLE TEMPERATURE MEASUREMENT METHODOLOGY USING THERMOGRAM AND VISIBLE-LIGHT IMAGE SETS,” pp. 1–9, 2022.

[8] C. K. Ho *et al.*, “Characterization of particle flow in a free-falling solar particle receiver,” *J. Sol. Energy Eng. Trans. ASME*, vol. 139, no. 2, pp. 1–9, 2017, doi: 10.1115/1.4035258.

[9] C. K. Ho and C. A. Pattyn, “Investigating environmental impacts of particle emissions from a high-temperature falling particle receiver,” *AIP Conf. Proc.*, vol. 2303, no. December, 2020, doi: 10.1063/5.0029219.

[10] M. Diago, A. C. Iniesta, A. Soum-Glaude, and N. Calvet, “Characterization of desert sand to be used as a high-temperature thermal energy storage medium in particle solar receiver technology,” *Appl. Energy*, vol. 216, no. October 2017, pp. 402–413, 2018, doi: 10.1016/j.apenergy.2018.02.106.

[11] J. D. Ortega, C. K. Ho, G. Anaya, P. Vorobieff, and G. Mohan, “The Application of a Non-Intrusive Methodology to Estimate Particle Egress Rate and Advective Heat Losses of a Falling Particle Receiver during On-Sun Tests,” *ASME J. Sol. Energy Eng.*, pp. 1–18.

[12] J. D. Ortega, “A Novel Imaging Methodology to Estimate Advective Losses from a Concentrating Solar Power Particle Receiver,” 2022.

[13] J. Ortega, G. Anaya, C. K. Ho, P. Vorobieff, and G. Mohan, “Bulk Velocity and Mass Flow Rate Estimation of Particle Plumes through PIV Analysis of Thermogram Sequences,” *J. Sol. Energy Eng.*, pp. 1–17, Apr. 2022, doi: 10.1115/1.4054358.

[14] J. Ortega, C. K. Ho, G. Anaya, P. Vorobieff, and G. Mohan, “A Non-Intrusive Particle Temperature Extraction Methodology using IR and Visible-Image Sequences for High-Temperature Particle Plumes,” *J. Sol. Energy Eng.*, pp. 1–23, 2022, doi: 10.1115/1.4055703.

[15] J. D. Ortega, G. Anaya, P. Vorobieff, C. K. Ho, and G. Mohan, “Particle plume velocities extracted from high-speed thermograms through particle image velocimetry,” *Proc. ASME 2021 15th Int. Conf. Energy Sustain. ES 2021*, pp. 1–6, 2021, doi: 10.1115/ES2021-63336.

[16] J. D. Ortega, C. K. Ho, and G. Anaya, “Bulk Velocity Extraction of a Particle Plume through Thermogram Correlation Velocimetry.” p. 1, 2020.

[17] K. Kim, N. Siegel, G. Kolb, V. Rangaswamy, and S. F. Moujaes, “A study of solid particle flow characterization in solar particle receiver,” *Sol. Energy*, vol. 83, no. 10, pp. 1784–1793, 2009, doi: 10.1016/j.solener.2009.06.011.

[18] G. Rottenkolber *et al.*, “Spray analysis of a gasoline direct injector by means of two-phase PIV,” *Exp. Fluids*, vol. 32, no. 6, pp. 710–721, 2002, doi: 10.1007/s00348-002-0441-8.

[19] L. Q. Ma, L. H. Feng, C. Pan, Q. Gao, and J. J. Wang, “Fourier mode decomposition of PIV data,” *Sci. China Technol. Sci.*, vol. 58, no. 11, pp. 1935–1948, 2015, doi: 10.1007/s11431-015-5908-y.

[20] E. W. R. Fisher, S. Perkins, A. Walker, “Image Transforms - Fourier Transform,” 2003. https://homepages.inf.ed.ac.uk/rbf/HIPR2/fourier.htm (accessed Oct. 23, 2020).

[21] O. Pust, “PIV: Direct Cross-Correlation compared with FFT-based Cross-Correlation,” pp. 1–12.

[22] W. Thielicke and E. J. Stamhuis, “PIVlab – Towards User-friendly, Affordable and Accurate Digital Particle Image Velocimetry in MATLAB,” *J. Open Res. Softw.*, vol. 2, 2014, doi: 10.5334/jors.bl.

[23] J. G. Santiago, S. T. Wereley, C. D. Meinhart, D. J. Beebe, and R. J. Adrian, “A particle image velocimetry system for microfluidics,” *Exp. Fluids*, vol. 25, no. 4, pp. 316–319, 1998, doi: 10.1007/s003480050235.

[24] C. R. Müller, J. F. Davidson, J. S. Dennis, and A. N. Hayhurst, “A study of the motion and eruption of a bubble at the surface of a two-dimensional fluidized bed using Particle image velocimetry (PIV),” *Ind. Eng. Chem. Res.*, vol. 46, no. 5, pp. 1642–1652, 2007, doi: 10.1021/ie0611397.

[25] B. W. Van Oudheusden, “PIV-based pressure measurement,” *Meas. Sci. Technol.*, vol. 24, no. 3, 2013, doi: 10.1088/0957-0233/24/3/032001.

[26] C. J. Kähler, U. Scholz, and J. Ortmanns, “Wall-shear-stress and near-wall turbulence measurements up to single pixel resolution by means of long-distance micro-PIV,” *Exp. Fluids*, vol. 41, no. 2, pp. 327–341, 2006, doi: 10.1007/s00348-006-0167-0.

[27] H. Wang, D. Liu, W. Gong, and L. Li, “Dynamic analysis of granite rockburst based on the PIV technique,” *Int. J. Min. Sci. Technol.*, vol. 25, no. 2, pp. 275–283, 2015, doi: 10.1016/j.ijmst.2015.02.017.

[28] K. T. Wu *et al.*, “Transition from turbulent to coherent flows in confined three-dimensional active fluids,” *Science (80-.).*, vol. 355, no. 6331, 2017, doi: 10.1126/science.aal1979.

[29] J. Oppenheimer, A. C. Rust, K. V. Cashman, and B. Sandnes, “Gas migration regimes and outgassing in particle-rich suspensions,” *Front. Phys.*, vol. 3, no. August, pp. 1–13, 2015, doi: 10.3389/fphy.2015.00060.

[30] S. Roman, C. Soulaine, M. A. AlSaud, A. Kovscek, and H. Tchelepi, “Particle velocimetry analysis of immiscible two-phase flow in micromodels,” *Adv. Water Resour.*, vol. 95, pp. 199–211, 2016, doi: 10.1016/j.advwatres.2015.08.015.

[31] J. D. Ortega, C. K. Ho, G. Anaya, P. Vorobieff, and G. Mohan, “A non-intrusive particle temperature measurement methodology using thermogram and visible-light image sets,” 2021, doi: 10.1115/ES2021-63791.

[32] J. D. Ortega, G. Anaya, P. Vorobieff, G. Mohan, and C. K. Ho, “Imaging Particle Temperatures and Curtain Opacities Using an IR Camera.” Jun. 17, 2020, doi: 10.1115/ES2020-1688.

[33] J. Cermak, I. F. Trigo, and J. Fuchs, “Imaging Techniques,” *Springer Handbooks*, no. 1, pp. 1175–1188, 2021, doi: 10.1007/978-3-030-52171-4_42.

[34] J. D. Ortega, I. R. Vazquez, P. Vorobieff, and C. K. Ho, “A simple and fast matlab-based particle size distribution analysis tool,” *Int. J. Comput. Methods Exp. Meas.*, vol. 9, no. 4, pp. 352–364, 2021, doi: 10.2495/CMEM-V9-N4-352-364.

[35] L. Yue, R. Shaeffer, B. Mills, and C. K. Ho, “Active airflow for reducing advective and particle loss in falling particle receivers,” *AIP Conf. Proc.*, vol. 2303, no. December, 2020, doi: 10.1063/5.0031223.

Appendix A

The following MATLAB script was implemented to obtain Figures 23-25.

```
clear all
close all
clc
directory='D:\UNM-Investigation\PIV MATLAB\DaVis\Diff_temp_comp';
suffix='*.dat';
direc = dir([directory,filesep,suffix]); filenames={};
[filenames{1:length(direc),1}] = deal(direc.name);
filenames = sortrows(filenames);

% read the dat file into matlab
%%%%%%%%%%%%%%%%%%%%%%%%%%%%%%%%%%%%%%%%%%%%%%%%%%%%%%%%%%%%%%%%%%%%%%%%%%%%%%%
% 5g single
data = dlmread(string(filenames(2)),' ',4,0);
data1 = dlmread(string(filenames(5)),' ',4,0);
data2 = dlmread(string(filenames(8)),' ',4,0);

% Find non zero velocity values
[rows]=find(data(:,4));
[rows1]=find(data1(:,4));
[rows2]=find(data2(:,4));
% temp=string(temp);
 Xp=(data(rows,1))-min(data(rows,1));

 Xp1=(data1(rows1,1))-min(data(rows1,1));

 Xp2=(data2(rows2,1))-min(data2(rows2,1));


M=data(rows,[1,2,4]);
M(:,1)=M(:,1)-min(M(:,1)); %x position
M(:,2)=M(:,2)-min(M(:,2)); %y position
M(:,3)=M(:,3)*-1;           %velocity

M1=data1(rows1,[1,2,4]);
M1(:,1)=M1(:,1)-min(M1(:,1)); %x position
M1(:,2)=M1(:,2)-min(M1(:,2)); %y position
M1(:,3)=M1(:,3)*-1;           %velocity

M2=data2(rows2,[1,2,4]);
M2(:,1)=M2(:,1)-min(M2(:,1)); %x position
M2(:,2)=M2(:,2)-min(M2(:,2)); %y position
M2(:,3)=M2(:,3)*-1;           %velocity

% Finding the mid line
Xp=sort(Xp);
M=sortrows(M);
A=Xp(round(length(M(:,1))./2)); %center line
D=Xp<=A+2;
C=Xp>=A-2;
```

```
B=find(C.*D);

ML=M(B(1):B(end),2:3);
ML=sortrows(ML);
ML(:,1)=(ML(:,1)-max(ML(:,1)))*-1;

clear A D C B
Xp1=sort(Xp1);
M1=sortrows(M1);
A=Xp1(round(length(M1(:,1))./2)); %center line
D=Xp1<=A+2;
C=Xp1>=A-2;
B=find(C.*D);

ML1=M1(B(1):B(end),2:3);
ML1=sortrows(ML1);
ML1(:,1)=(ML1(:,1)-max(ML1(:,1)))*-1;

clear A D C B
Xp2=sort(Xp2);
M2=sortrows(M2);
A=Xp2(round(length(M2(:,1))./2)); %center line
D=Xp2<=A+2;
C=Xp2>=A-2;
B=find(C.*D);

ML2=M2(B(1):B(end),2:3);
ML2=sortrows(ML2);
ML2(:,1)=(ML2(:,1)-max(ML2(:,1)))*-1;

% Ploting mid line
figure
vref=sqrt((2*ML(:,1)./1000)*9.81);
plot(ML(:,1)./1000,vref,'k','Linewidth',2)
hold on
plot(ML(3:end,1)./1000,ML(3:end,2),'b','Linewidth',2)
plot(ML1(:,1)./1000,ML1(:,2),'color','#EDB120','Linewidth',2)
plot(ML2(:,1)./1000,ML2(:,2),'r','Linewidth',2)
xlabel('Y Position (m)','FontSize',20)
ylabel('Velocity (m/s)','FontSize',20)
grid minor
title({'Particles Velocity Vs Free Fall, Single Flow';...
    '5 g/s, Center Line, Diff. Temperature'},'FontSize',18)
lgn=legend('Free Fall','100 \circC','450 \circC','750 \circC','FontSize',14);
lgn.Location='southeast';
dim = [.2 .5 .3 .3];
str = 'DaVis data';
annotation('textbox',dim,'String',str,'FitBoxToText','on');
axis([0 max(ML(:,1))./1000 0 3])
set(gcf,'units','inches','position',[1 1 5.5 5])
print(gcf,'-r900','-dtiff','DaVis5gsingle.tiff')
%%%%%%%%%%%%%%%%%%%%%%%%%%%%%%%%%%%%%%%%%%%%%%%%%%%%%%%%%%%%%%%%%%%%%%%%%%%%%%%
% 0.5g single flow
clear M M1 M2 ML ML1 ML2 rows rows1 rows2 data data1 data2 Xp Xp1 Xp2
```

```
data = dlmread(string(filenames(1)),' ',4,0);
data1 = dlmread(string(filenames(4)),' ',4,0);
data2 = dlmread(string(filenames(7)),' ',4,0);

% Find non zero velocity values
[rows]=find(data(:,4));
[rows1]=find(data1(:,4));
[rows2]=find(data2(:,4));
% temp=string(temp);
 Xp=(data(rows,1))-min(data(rows,1));

 Xp1=(data1(rows1,1))-min(data(rows1,1));

 Xp2=(data2(rows2,1))-min(data2(rows2,1));


M=data(rows,[1,2,4]);
M(:,1)=M(:,1)-min(M(:,1)); %x position
M(:,2)=M(:,2)-min(M(:,2)); %y position
M(:,3)=M(:,3)*-1;           %velocity

M1=data1(rows1,[1,2,4]);
M1(:,1)=M1(:,1)-min(M1(:,1)); %x position
M1(:,2)=M1(:,2)-min(M1(:,2)); %y position
M1(:,3)=M1(:,3)*-1;           %velocity

M2=data2(rows2,[1,2,4]);
M2(:,1)=M2(:,1)-min(M2(:,1)); %x position
M2(:,2)=M2(:,2)-min(M2(:,2)); %y position
M2(:,3)=M2(:,3)*-1;           %velocity

% Finding the mid line
Xp=sort(Xp);
M=sortrows(M);
A=Xp(round(length(M(:,1))./2)); %center line
D=Xp<=A+2;
C=Xp>=A-2;
B=find(C.*D);

ML=M(B(1):B(end),2:3);
ML=sortrows(ML);
ML(:,1)=(ML(:,1)-max(ML(:,1)))*-1;

clear A D C B
Xp1=sort(Xp1);
M1=sortrows(M1);
A=Xp1(round(length(M1(:,1))./2)); %center line
D=Xp1<=A+2;
C=Xp1>=A-2;
B=find(C.*D);

ML1=M1(B(1):B(end),2:3);
ML1=sortrows(ML1);
ML1(:,1)=(ML1(:,1)-max(ML1(:,1)))*-1;
```

```
clear A D C B
Xp2=sort(Xp2);
M2=sortrows(M2);
A=Xp2(round(length(M2(:,1))./2)); %center line
D=Xp2<=A+2;
C=Xp2>=A-2;
B=find(C.*D);

ML2=M2(B(1):B(end),2:3);
ML2=sortrows(ML2);
ML2(:,1)=(ML2(:,1)-max(ML2(:,1)))*-1;
% ML(:,2)=ML(:,2)-max(ML(:,2));
% Ploting mid line
figure
vref=sqrt((2*ML(:,1)./1000)*9.81);
plot(ML(:,1)./1000,vref,'k','Linewidth',2)
hold on
plot(ML(3:end,1)./1000,ML(3:end,2),'b','Linewidth',2)
plot(ML1(:,1)./1000,ML1(:,2),'color','#EDB120','Linewidth',2)
plot(ML2(:,1)./1000,ML2(:,2),'r','Linewidth',2)
xlabel('Y Position (m)','FontSize',20)
ylabel('Velocity (m/s)','FontSize',20)
grid minor
title({'Particles Velocity vs Free Fall, Single Flow';...
    '0.5 g/s, Center Line, Diff. Temperatures'},'FontSize',18)
lgn=legend('Free Fall','100 \circC','450 \circC','700 \circC','FontSize',14);
lgn.Location='southeast';
dim = [.2 .5 .3 .3];
str = 'DaVis data';
annotation('textbox',dim,'String',str,'FitBoxToText','on');
axis([0 max(ML(:,1))./1000 0 3])
set(gcf,'units','inches','position',[1 1 5.5 5])
print(gcf,'-r900','-dtiff','DaVis05gsingle.tiff')
%%%%%%%%%%%%%%%%%%%%%%%%%%%%%%%%%%%%%%%%%%%%%%%%%%%%%%%%%%%%%%%%%%%%%%%%%%%%%%%
% 5g slpit flow
clear M M1 M2 ML ML1 ML2 rows rows1 rows2 data data1 data2 Xp Xp1 Xp2
data = dlmread(string(filenames(3)),' ',4,0);
data1 = dlmread(string(filenames(6)),' ',4,0);
data2 = dlmread(string(filenames(9)),' ',4,0);

% Find non zero velocity values
[rows]=find(data(:,4));
[rows1]=find(data1(:,4));
[rows2]=find(data2(:,4));
% temp=string(temp);
 Xp=(data(rows,1))-min(data(rows,1));

 Xp1=(data1(rows1,1))-min(data(rows1,1));

 Xp2=(data2(rows2,1))-min(data2(rows2,1));

M=data(rows,[1,2,4]);
M(:,1)=M(:,1)-min(M(:,1)); %x position
```

```
M(:,2)=M(:,2)-min(M(:,2)); %y position
M(:,3)=M(:,3)*-1;           %velocity

M1=data1(rows1,[1,2,4]);
M1(:,1)=M1(:,1)-min(M1(:,1)); %x position
M1(:,2)=M1(:,2)-min(M1(:,2)); %y position
M1(:,3)=M1(:,3)*-1;           %velocity

M2=data2(rows2,[1,2,4]);
M2(:,1)=M2(:,1)-min(M2(:,1)); %x position
M2(:,2)=M2(:,2)-min(M2(:,2)); %y position
M2(:,3)=M2(:,3)*-1;           %velocity

% Finding the mid line
Xp=sort(Xp);
M=sortrows(M);
A=Xp(round(length(M(:,1))./2)); %center line
D=Xp<=A+2;
C=Xp>=A-2;
B=find(C.*D);

ML=M(B(1):B(end),2:3);
ML=sortrows(ML);
ML(:,1)=(ML(:,1)-max(ML(:,1)))*-1;

clear A D C B
Xp1=sort(Xp1);
M1=sortrows(M1);
A=Xp1(round(length(M1(:,1))./2)); %center line
D=Xp1<=A+2;
C=Xp1>=A-2;
B=find(C.*D);

ML1=M1(B(1):B(end),2:3);
ML1=sortrows(ML1);
ML1(:,1)=(ML1(:,1)-max(ML1(:,1)))*-1;

clear A D C B
Xp2=sort(Xp2);
M2=sortrows(M2);
A=Xp2(round(length(M2(:,1))./2)); %center line
D=Xp2<=A+2;
C=Xp2>=A-2;
B=find(C.*D);

ML2=M2(B(1):B(end),2:3);
ML2=sortrows(ML2);
ML2(:,1)=(ML2(:,1)-max(ML2(:,1)))*-1;
% ML(:,2)=ML(:,2)-max(ML(:,2));
% Ploting mid line
figure
plot(ML(:,1)./1000,ML(:,2),'b','Linewidth',2)
hold on
plot(ML1(:,1)./1000,ML1(:,2),'color','#EDB120','Linewidth',2)
```

```
plot(ML2(:,1)./1000,ML2(:,2),'r','Linewidth',2)
syms y
vrefy=sqrt((2*y)*9.81);
fplot(vrefy,'k','Linewidth',2)
xlabel('Discharge position (m)','FontSize',18)
ylabel('Velocity (m/s)','FontSize',18)
grid minor
title({'Particles Velocity vs Free Fall, Split Flow';...
    '5 g/s, Center Line, Diff. Temperatures'},'FontSize',18)
lgn=legend('100\circC',...
    '450\circC',...
    '750\circC','Free-Fall','FontSize',14);
lgn.Location='southeast';
dim = [.2 .5 .3 .3];
str = 'DaVis data';
%
annotation('textbox',dim,'String',str,'FitBoxToText','on');
%}
axis([0 max(ML(:,1))./1000 0 3])
set(gcf,'units','inches','position',[1 1 5.5 5])
print(gcf,'-r900','-dtiff','DaVis5gsplit.tiff')
%%%%%%%%%%%%%%%%%%%%%%%%%%%%%%%%%%%%%%%%%%%%%%%%%%%%%%%%%%%%%%%%%%%%%%%%%%%%%%%
```

Published with MATLAB® R2020a